

1 **Evaluation of aerosol optical depths and clear-sky radiative fluxes of the**
2 **CERES Edition 4.1 SYN1deg data product**

3
4

5 David W. Fillmore¹, David A. Rutan², Seiji Kato³, Fred G. Rose²,
6 and Thomas E. Caldwell²

7

8 ¹University Center for Atmospheric Research, Boulder, CO. 80307, USA

9 ²SSAI, Hampton, VA, 23666, USA

10 ³NASA Langley Research Center, Hampton, VA, 23666, USA

11

12

13

14

Submitted to

15

Atmospheric Chemistry and Physics

16

April 2021

17

18

19

20

21

22 *Corresponding author address:* David W Fillmore,
23 University Center for Atmospheric Research
24 P.O. Box 3000
25 Boulder, CO 80307
26 E-mail: david.w.fillmore@ucar.edu

27 Abstract

28 Aerosol optical depths (AOD) used for the Edition 4.1 Clouds and the Earth's Radiant
29 Energy System (CERES) Synoptic (SYN1deg) are evaluated. AODs are derived from
30 Moderate Resolution Imaging Spectroradiometer (MODIS) observations and assimilated
31 by an aerosol transport model (MATCH). As a consequence, clear-sky AODs closely
32 match with those derived from MODIS instruments. AODs under all-sky conditions are
33 larger than AODs under clear-sky conditions, which is supported by ground-based
34 AERONET observations. When all-sky MATCH AODs are compared with Modern-Era
35 Retrospective Analysis for Research and Applications (MERRA2) AODs, MATCH
36 AODs are generally larger than MERRA2 AODS especially over convective regions (e.g.
37 Amazon, central Africa, and eastern Asia). The difference is due to the differing methods
38 of assimilating the MODIS AOD data product and the use of quality flags in our
39 assimilation-largely caused by MODIS AODs used for assimilation. Including AODs
40 with larger retrieval uncertainty makes AODs over the convective regions larger. When
41 AODs are used for clear-sky irradiance computations and computed downward
42 shortwave irradiances are compared with ground-based observations, the computed
43 instantaneous irradiances are 1% to 2% larger than observed irradiances. The comparison
44 of top-of-atmosphere clear-sky irradiances with those derived from CERES observations
45 suggests that AODs used for surface radiation observation sites are larger by 0.01 to 0.03,
46 which is within the uncertainty of instantaneous MODIS AODs. However, the
47 comparison with AERONET AOD suggests AODs used for computations over desert
48 sites are 0.08 larger. The cause of positive biases of downward shortwave irradiance and
49 positive bias in AOD for the desert sites is possibly due to dust particle size and their

50 distribution as defined by the MATCH transport model and the transfer of that
51 information into the radiative transfer model.

52 ~~However, the comparison with AERONET AOD suggests AODs used for computations~~
53 ~~over desert sites are 0.08 larger. The cause of positive biases of downward shortwave~~
54 ~~irradiance and AODs for the desert sites is under investigation.~~

57 **1. Introduction**

58 Accurate estimates of the radiative effects of clouds and aerosols are essential for
59 an understanding the radiative forcing to the Earth's climate system (Bauer and Menon,
60 2012, Boucher et al. 2013). In addition, through the reflection and absorption of solar
61 radiation, and the absorption and emission of terrestrial thermal radiation, clouds and
62 aerosols affect the radiative heating of both the atmosphere and the surface, which in turn
63 governs the atmospheric circulation and the hydrological cycle (e.g. Stephens et al. 2020,
64 L'Ecuyer et al. 2015). Under the Earth Observing System (EOS) program, the National
65 Aeronautics and Space Administration (NASA) has placed into orbit a series of satellites
66 devoted to long term observations of the climate state. Among these are Terra and Aqua,
67 the flagship satellites of the EOS. Central to observation of climate evolution are
68 Moderate Resolution Imaging Spectroradiometer (MODIS) and the Clouds and the
69 Earth's Radiant Energy System (CERES) instrument pairs that fly on both the Terra
70 (March 2000 - present) and the Aqua (July 2002 - present) platforms (Wielicki et al.
71 1996). Additional CERES instruments were launched (October 2011) upon the Suomi
72 National Polar-orbiting Partnership (NPP) satellite along with the MODIS successor, the

73 Visible Infrared Imager Radiometer Suite (VIIRS), and on the NOAA-20 satellite
74 (November 2017). In addition to observations from these satellites, the CERES mission
75 also integrates observations from the Geostationary Operational Environmental Satellites
76 (GOES) (West and East), as well as other geostationary satellites around the globe, for
77 full diurnal coverage of clouds and radiation.

78 The CERES instruments measure broadband radiances over the solar spectrum
79 (shortwave), the thermal infrared (longwave radiance is obtained from a total channel
80 minus the shortwave channel), and the near infrared atmospheric window, with frequent
81 on-board calibration. CERES measurements, in conjunction with MODIS information,
82 are used to infer broadband irradiances through empirical angular distribution models
83 (ADMs). Geosynchronous satellite imagery observes the diurnal cycle of clouds, which is
84 not fully sampled by the polar orbiting satellites upon which CERES and MODIS reside.

85 While top-of-atmosphere (TOA) irradiances are derived from broadband
86 radiances measured by CERES instruments (Loeb et al. 2005; Su et al. 2015), surface and
87 in atmosphere irradiances are computed with a radiative transfer model. Inputs used for
88 the computations include cloud properties derived from MODIS and geostationary
89 satellites, aerosol optical depth derived from MODIS radiances, and surface albedo
90 derived from MODIS and CERES observations (Rutan et al. 2009). Temperature and
91 humidity profiles are provided by a reanalysis product produced by the NASA Goddard
92 Modeling and Assimilation Office (GMAO).

93 Irradiances at the surface produced by the CERES team have been compared with
94 surface observations (Rutan et al. 2015; Kato et al. 2013, 2018). These comparisons are
95 for all-sky conditions (i.e. including any clouds). Irradiances under clear-sky conditions

96 are not explicitly separated from all-sky conditions in the evaluations. There are several
97 reasons that impede efforts at rigorous validation of clear-sky irradiances with surface
98 observations; 1) a clear-sky condition at a given site does not persist over a long time
99 (e.g. a month or longer), 2) there are mismatches of clear-sky conditions determined by
100 satellite- and ground-based instruments, and 3) field-of-view size between CERES
101 instruments and ground-based radiometers differ.

102 Despite difficulties in evaluating computed clear-sky irradiances, they play an
103 important role in quantifying aerosol and cloud radiative effects (Loeb and Su 2010;
104 Soden and Chung 2017). Therefore, the uncertainty in surface irradiances need to be
105 understood in order to assess the uncertainty in aerosol and cloud radiative effect. This
106 work is the first attempt by the CERES team to evaluate clear-sky surface irradiances
107 provided by its data products. One of the essential variables in computing clear-sky
108 irradiances is aerosol optical depth. In this paper, we evaluate aerosol optical depth used
109 for irradiance computations in the CERES project and analyze how the error propagates
110 to clear-sky surface irradiances. Computations of surface irradiances provided by Edition
111 4.1 SYN1deg data products use aerosol optical depth derived by a chemical transport
112 model [The Model for Atmospheric Transport and Chemistry (MATCH, Collins et al.
113 2001)] that assimilates MODIS-derived aerosol optical depth. In Section 2, we explain in
114 the MATCH aerosol transport model and the assimilation of aerosol optical depth with
115 MODIS. We then compare MATCH AOD to MODIS and MERRA2 aerosol products, as
116 well as to AOD from the Aerosol Robotic Network (AERONET, Holben et al. 1998).
117 Section 3 discusses differences found between the various estimates of AOD. Section 4
118 looks at clear sky surface irradiance calculations from the SYN1deg product compared to

119 observed values and the impact of AOD and particle size on the results. Conclusions are
120 presented in section 5.

121

122

123 **2. Description of MATCH model**

124 The Model for Atmospheric Transport and Chemistry (MATCH) is a transport
125 model of intermediate complexity driven by offline meteorological fields from the
126 National Centers for Environmental Prediction (NCEP) reanalysis. It is run on a 194×96
127 (1.9°×1.9°) spatial grid with a vertical resolution of 28 sigma-p levels. Temporally, the
128 meteorological fields are linearly interpolated to 30-minute times at which time the
129 chemical processes are run. One exception is that the sulfur model is interpolated again to
130 run at 2-min subscale time steps. MATCH is one of the many aerosol transport models
131 that participated in the AeroCom model inter-comparison project (Textor et al., 2006;
132 Kinne et al. 2006; Textor et al. 2007) and the AeroCom carbon inter-comparison project
133 (Koch et al., 2009; Huneus et al., 2011).

134 Aerosol types included in MATCH are dust, sulfate, sea salt, soot, sulfates,
135 carbon, and volcanic particles (**Table 1**). Model physics included in MATCH are
136 parameterizations for convection and boundary layer processes that include prognostic
137 cloud and precipitation schemes for aqueous chemistry and the scavenging of soluble
138 species. MATCH also includes the ability to resolve the transport of aerosols via
139 convection, boundary layer transport, and scavenging and deposition of soluble gases and
140 aerosols. MATCH can simulate most cloud processes currently in use in a GCM (eg.
141 cloud fraction, cloud water and ice content, fraction of water converted to rain and snow,

142 and evaporation of condensate and precipitate). It also includes vertical turbulent eddy
 143 processes. These processes are then used for convective transport, wet scavenging, wet
 144 deposition and dry deposition of the MATCH aerosols. These various parameterizations
 145 were developed, originally, for the NCAR Community Climate Model (CCM) and
 146 subsequently incorporated into the MATCH model. Descriptions of these
 147 parameterizations are given by Rasch et. al (1997, 2001), Collins et. al (2001) and
 148 additional papers described therein.

149 The MATCH aerosol suite includes a detailed mineral dust scheme in the Dust
 150 Entrainment and Deposition model, (Zender et al., 2003), and a diagnostic
 151 parameterization for sea-salt aerosol based on the 10m wind speed (Blanchard and
 152 Woodcock, 1980). The sulfur cycle and the chemical reactions for sulfate aerosol creation
 153 rely on monthly climatological oxidant fields and emission inventories (**Table 1**) for
 154 sulfur oxides and oceanic dimethyl sulfide (photochemistry and nitrate aerosol are
 155 omitted). The reaction scheme is similar to that of the Model for Ozone and Related
 156 Chemical Tracers (MOZART), (Emmons et al., 2010). Carbon aerosols (both organic
 157 compounds and soot) evolve with simple mean lifetime e-foldings from surface fluxes
 158 specified through natural, biomass burning and fossil fuel burning emission inventories
 159 (also monthly climatologies given in **Table 1**).

Table 1. Aerosol Types & Climatological Sources

<i>Aerosol Type</i>	<i>Source</i>	<i>Description</i>
<i>Sea Salt</i>	Blanchard and Woodcock, 1980	Wind Driven
<i>Dust</i>	Ginoux et al. (2001); Zender et al. (2003)	NCEP soil moisture, wind driven

<i>Sulfate (natural & anthropogenic)</i>	Benkovitz et al. (1996); Barth et al. (2000)	monthly climatological
<i>Carbon (organic & Soot)</i>	Lioussé et al. (1996)	monthly climatological
<i>Volcanic</i>	Episodic inclusion of Sulfur dioxide	Processed by model

160

161

162

163

164

165

166

167

168

169

170

171

The optical properties of the various aerosol types (e.g. mass extinction coefficient, single scatter albedo), which are key parameters for aerosol assimilation, are drawn from the standard Optical Properties of Clouds and Aerosols (OPAC, Hess et al. 1998) database. However, scattering properties of maritime and dust aerosols used in the radiative transfer calculations in the SYN1deg are not from MATCH. Instead, aerosol types from MATCH are mapped to a similar set of scattering properties, per Table 2, embedded in the Langley Fu & Liou radiative transfer (LFLRT) code (Fu and Liou, 1993; Fu et. al 1998; Rose et. al 2013). These include OPAC as in MATCH for all but the small and large dust particles. Dust scattering and absorption properties in the LFLRT code are from Sinyuk et al. (2003).

Table 2. Mapping of MATCH aerosol types into Radiative Transfer code.

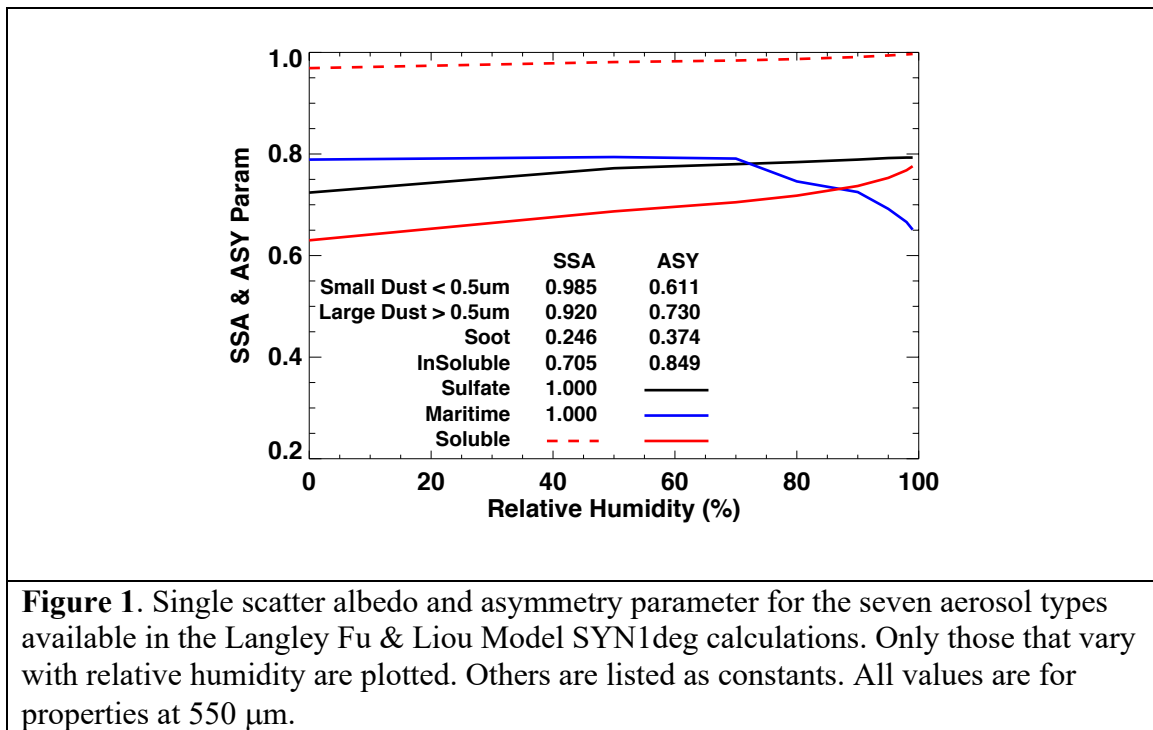
MATCH Constituent	Langley Fu & Liou Constituent	Langley Fu & Liou Spectral Properties
Sea Salt	Maritime	d’Almeida 1991
Hydrophobic Organic Carbon	Insoluble	OPAC
Hydrophilic Black Carbon	Soot	OPAC
Hydrophobic Black Carbon		
Hydrophilic Organic Carbon	Water Soluble (WASO)	OPAC
Tropospheric Sulfate		
Volcanic	Suspended Organic (SUSO)	OPAC
Stratospheric Sulfate		
Dust < 1.0µm	“Small” Dust	Sinyuk et al. (2003)
Dust 1.0 -2.5µm	“Large” Dust	Sinyuk et al. (2003)

Dust 2.5-5.0 μm		
Dust 5.0-10.0 μm		

172

173

174 **Figure 1** shows the single scatter albedo (SSA) and asymmetry parameter (ASY)
 175 for the seven constituents in the LFLRT code at 500 μm . Constituents with constant SSA
 176 and/or ASY are given as numbers while those that vary with relative humidity are
 177 plotted. The spectral properties for sea salt shown in Figure 1 were taken directly from
 178 tables in d’Almeida et al., (1991). Note that the asymmetry parameter of maritime
 179 aerosol decreases with humidity. This is likely an error in the original Table A.30 of
 180 d’Almeida et al. (1991).



181

182

2.1 MATCH Assimilation of MODIS Aerosol Optical Depths

183 One major advantage of the MATCH model is its ability to reliably assimilate
184 satellite-based retrievals of aerosol optical depth (AOD) to constrain the climatologically
185 forced aerosols generated within the chemical transport portion of the code. Edition 4
186 MATCH algorithms ingest MODIS Collection 6.1 AOD (Remer et al., 2005), beginning
187 in March 2000 from the Terra satellite and June 2002 from both Terra and Aqua
188 satellites. The MATCH assimilates MODIS AOD at the green wavelength of 550 nm.
189 MATCH combines AOD derived by the Dark Target (Levy et al. 2013) and Deep Blue
190 algorithms (Hsu et al., 2006). A global daily mean AOD in a $1.9^\circ \times 1.9^\circ$ grid is derived
191 from Terra and Aqua observations by simply averaging available Terra and Aqua dark
192 target and deep blue derived AODs in a grid box. Unlike dark target and deep blue
193 merged product (MOD08), we do not use a quality assurance confidence (QAC) score to
194 screen AOD.

195 The assimilation process begins by combining the dark target and deep blue AOD
196 from MODIS (both Terra and Aqua when available) and creating daily averages. As
197 MATCH progresses through time the AOD at local solar noon are assimilated by taking a
198 15° longitude width of retrieved AOD from the daily mean map. Examples of the
199 magnitude of AOD adjustments by the assimilation are shown in **Fig. 2. Figure 2a** shows
200 hourly AOD field differences, 4 UT minus 3 UT on February 1st, 2020. Similarly, **Figure**
201 **2b** shows 10 UT minus 9 UT of the same day. The 15° vertical band is clearly visible
202 where red (blue) colors indicate total column aerosol is increased (decreased) by the
203 MODIS AOD assimilation. Following the AOD adjustment, aerosol masses in the
204 atmospheric column through the troposphere are scaled to closely match the AOD
205 derived from MODIS. Neither the vertical profile nor the relative abundance of the

206 aerosol species is adjusted. Once aerosol mass is adjusted at the local noon for the regions
 207 where MODIS AOD is available, the adjusted aerosol mass is carried on to the next time
 208 step. Besides the MODIS adjustments, wind driven sea-salt creation and deposition are
 209 found along frontal boundaries in the North Atlantic and Southern Oceans. The maps also
 210 indicate hourly increases and decreases in high aerosol loading areas such as those found
 211 around China and SE Asia. Episodic events such as intense fires or volcanic eruptions
 212 are not specifically included in the MATCH aerosol package. Such events are captured
 213 by the assimilation of MODIS AOD and total column aerosol loading is adjusted upward.
 214 The adjustment is applied to AOD only. The aerosol type (and so scattering properties) is
 215 not adjusted to reflect the reality of the scattering or absorbing aerosol during such an
 216 event.

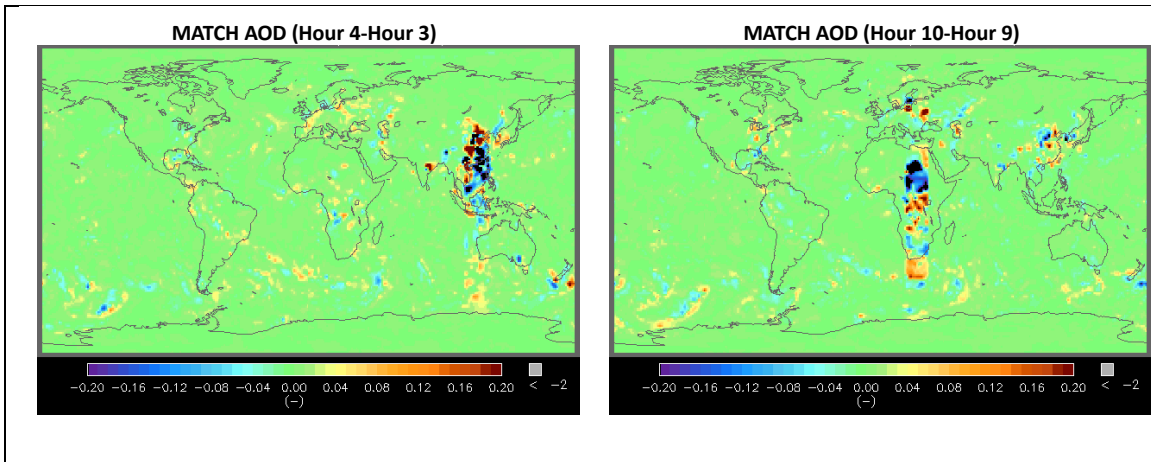


Figure 2. Difference of MATCH AOD due to the assimilation of MODIS AOD. The left plot is 4 UT minus 3 UT and right plot is 10 UT minus 9 UT on February 1, 2020. AOD is adjusted at the local solar noon within the 15° longitudinal band by the MODIS AOD assimilation. Wind-blown dust and sea salts differences are also apparent outside the 15° longitudinal band.

217

218 **2.2 MATCH and MERRA2 comparison**

219 In this section, we compare AODs between MATCH and MERRA2 (Randles et

220 al., 2017) in which MODIS clear-sky radiances are assimilated. MERRA2 also

221 assimilates surface observed AOD by AERONET and ship born AOD observations as
 222 well as AVHRR and MISR retrievals for the years 2000-2002 and 2000-2014
 223 respectively. We compare AODs in two different ways. First, MATCH and MERRA2
 224 AODs are compared with MODIS AODs. The first comparison tests the consistency of
 225 daily means when MODIS aerosol optical depth is available (i.e. clear somewhere in the
 226 grid box at Terra and Aqua overpass time). Second, MATCH and MERRA2 AODs are
 227 compared under all-sky conditions, which is only possible with modeled AODs.

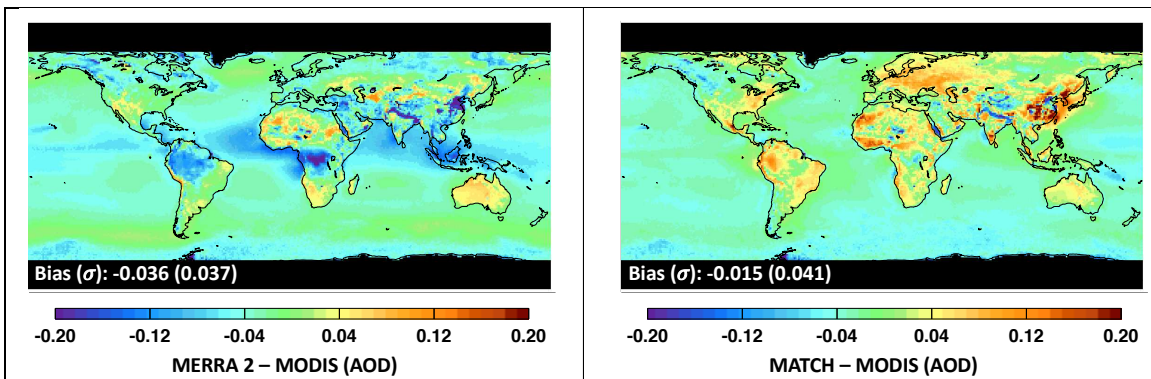


Figure 3: Climatological mean aerosol optical depth (AOD, i.e. $\langle AOD_{MODIS}^{clr} \rangle$ see texts for the definition) difference of left) MERRA2 – MODIS and right) MATCH – MODIS averaged over Mar 2000 through Feb 2020. MERRA2 and MATCH daily mean AODs are sampled when daily mean MODIS AOD from the same $1^\circ \times 1^\circ$ grid is available. Sampled daily mean AODs are subsequently averaged. MODIS AODs are averages of MODIS dark target and deep blue algorithms from both Terra (MOD08) and Aqua (MYD08) data products.

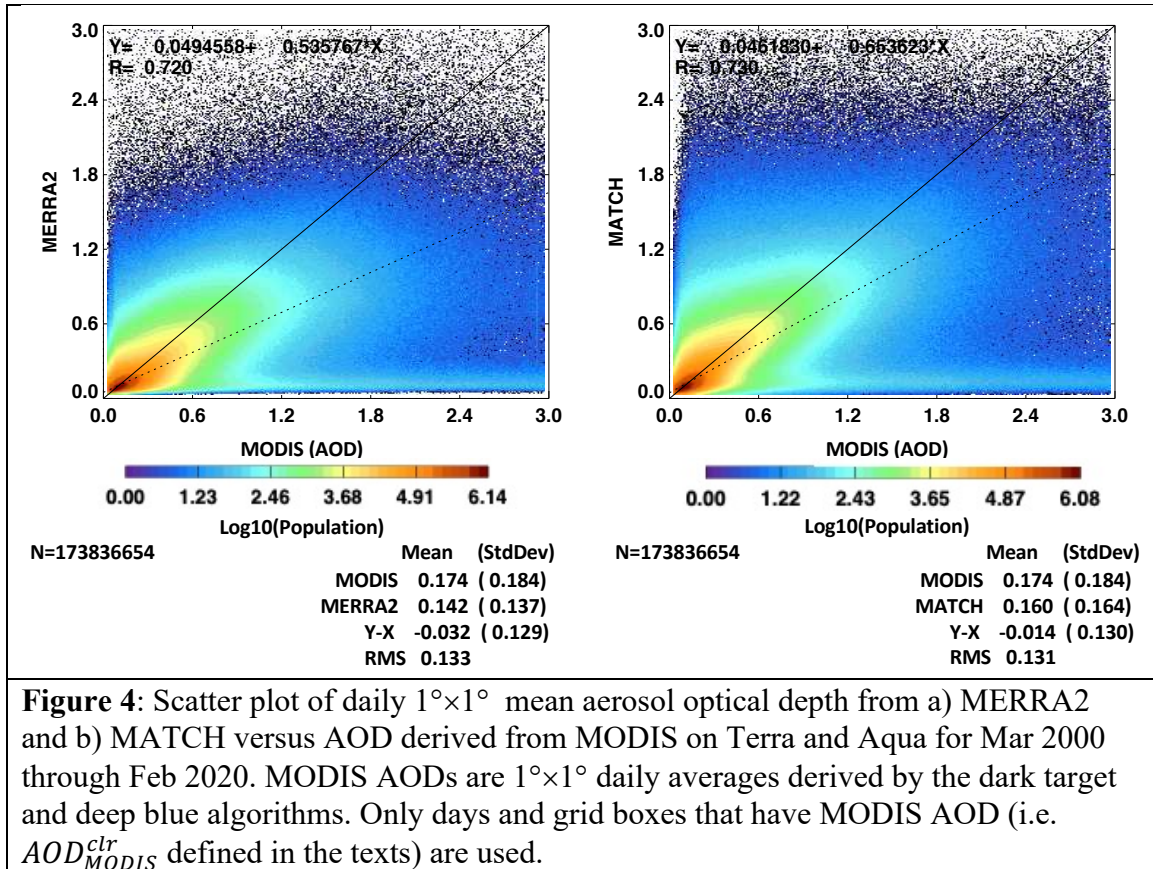
228
 229 **Figure 3** shows differences of climatological mean AOD between MERRA2 and
 230 MODIS on the left and MATCH and MODIS on the right. To compute the monthly mean
 231 AOD differences, both MERRA2 and MATCH daily mean AODs are sampled when
 232 daily mean MODIS AOD (MODIS products MOD08 and MYD08) from the same $1^\circ \times 1^\circ$
 233 grid is available (hereinafter AOD_{MODIS}^{clr}). Sampled daily mean AODs (AOD_{MODIS}^{clr}) are
 234 subsequently averaged (hereinafter $\langle AOD_{MODIS}^{clr} \rangle$, where the bracket indicates a simple
 235 arithmetic mean). Although both products assimilate MODIS observations, each shows

236 fairly significant differences from MODIS values. Differences arise because MODIS
237 daily mean AOD is clear sky at Terra and Aqua overpass time while MERRA2 and
238 MATCH daily mean AOD includes AOD from other times of the day. When the non-
239 overpass time is also clear, MATCH AOD_{MODIS}^{clr} should be close to MODIS AOD_{MODIS}^{clr} .
240 However, when clouds are present in MATCH during non-overpass times, modeled AOD
241 are used, hence the daily mean AOD can deviate from MODIS AOD_{MODIS}^{clr} . In addition,
242 AOD differences for MERRA2 at Terra and Aqua overpass times might be larger than
243 MATCH even for clear-sky conditions as MERRA2 assimilates observed AOD data
244 other than MODIS AOD when and where these events might occur.

245 While MATCH shows large positive differences over land, especially China and
246 southeast Asia, Australia, Amazon, and north Africa, MERRA2 shows significant
247 negative differences over major rain-forest regions of south America, Africa, and the
248 tropical western Pacific. Both products are closer to MODIS AOD over ocean compared
249 to $\langle AOD_{MODIS}^{clr} \rangle$ over land except MERRA2 shows a negative difference across the Indian
250 ocean and off the west coast of Africa in the Atlantic Ocean. When MODIS AOD_{MODIS}^{clr} is
251 available in the grid box, MATCH weighs MODIS AOD heavily in its assimilation at
252 local solar noon so that MATCH AOD is nearly identical to MODIS AOD at the local
253 noon under clear-sky regions. Consequently, the difference of climatological global mean
254 MATCH and MODIS AOD_{MODIS}^{clr} (-0.015) is smaller than the difference of MERRA2 and
255 MODIS AOD_{MODIS}^{clr} (-0.036).

256 **Figure 4** shows the difference of AOD_{MODIS}^{clr} more clearly. In **Fig. 4** AOD_{MODIS}^{clr} are
257 compared directly in a log-density plot where each point represents a comparison for the
258 daily average of a given grid box; MERRA2 versus MODIS on the left and MATCH

259 versus MODIS on the right. **Figure 4** indicates that MATCH AOD_{MODIS}^{clr} has a smaller
 260 bias with respect to the MODIS AOD than the MERRA2 AOD but has approximately the
 261 same RMS compared to the MERRA2 AOD_{MODIS}^{clr} .
 262
 263



264
 265
 266 We now consider more directly, differences between the MATCH and MERRA2
 267 climatological AOD fields for all-sky and *estimated* clear sky conditions. **Figure 5** shows
 268 $1^\circ \times 1^\circ$ climatological mean maps of MATCH AOD on the left and its difference from
 269 MERRA2 on the right for all sky (top maps) and estimated clear sky (bottom maps)
 270 conditions for March 2000 through February 2020. A clear-sky area weighted monthly
 271 mean aerosol optical depth is derived by averaging daily mean aerosol optical depth

272 weighted by clear fraction (hereinafter $\overline{AOD_{MODIS}^{clr}}$, overbar indicates monthly mean),
 273 where the clear fraction is derived from MODIS on Terra and Aqua (Loeb et al. 2020,
 274 Minnis et al. 2020). MATCH all-sky AOD (hereinafter $\overline{AOD^{all}}$) is larger than MERRA2
 275 $\overline{AOD^{all}}$, particularly over the rain forest regions of the globe as well as India and China.
 276 Although the difference is smaller, the difference of $\overline{AOD_{MODIS}^{clr}}$ shows a similar spatial
 277 pattern (**Fig. 5** bottom right) to the all-sky difference. This is consistent with **Fig. 3**,
 278 showing that MERRA2 AOD_{MODIS}^{clr} underestimates AOD with respect to MODIS
 279 AOD_{MODIS}^{clr} . A larger difference in MATCH AOD over convective regions (e.g. Amazon,
 280 central Africa, and south east Asia) is caused by how dark target and deep blue AOD are
 281 merged. As mentioned earlier, we do not use QAC to screen AOD. Convective clouds
 282 introduce a larger uncertainty to AOD because of a 3D radiation effect or poor fit to
 283 observations with retrieved AOD (personal communication with R. Levy 2020). For
 284 these situations, AODs associated with QA confidence scores less than 2 are screened out
 285 in the MOD08 dark target and deep blue merged product (Levy et al. 2013).

286 **2.3 Comparison with AERONET**

287 The above results indicate that both MATCH AOD_{MODIS}^{clr} and MERRA2
 288 $\overline{AOD_{MODIS}^{clr}}$ are generally smaller than MODIS $\overline{AOD_{MODIS}^{clr}}$. Larger difference between
 289 MATCH and MERRA2 $\overline{AOD^{all}}$ over convective regions originated from merged AOD
 290 product used for the assimilation. Of primary importance to radiative transfer calculations
 291 within the SYN1deg product is the ability of the MATCH model to accurately represent
 292 total column aerosol optical depth. To test the overall accuracy, we use observations from
 293 the AERosol RObotic NETwork (AERONET). AERONET is a global federation of
 294 ground-based remotes sensing sites developed by NASA and now supported by a number

295 of institutions around the world (Holben et al. 1998). Each site maintains a CIMEL sun-
 296 photometer that scans the daytime sky every 20 minutes. Collected data are processed
 297 according to standards of calibration and processing maintained by the AERONET
 298 project. Here we utilize Level 2.0, data that have been screened for clouds and quality
 299 assured (Smirnov et al. 2000).
 300

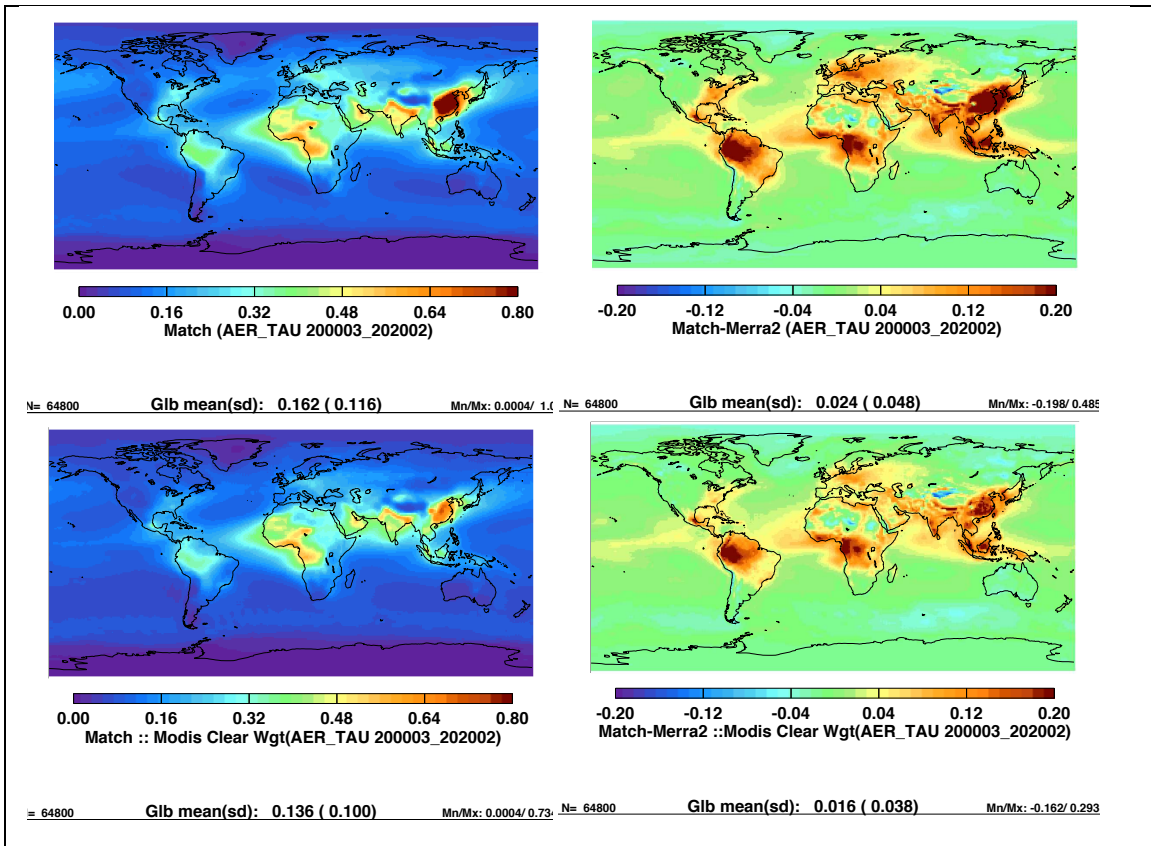


Figure 5. Left) Climatological mean AOD from MATCH and right) the difference between MATCH and MERRA2 (MATCH – MERRA2). Top maps are for all-sky (AOD_{MODIS}^{all}), bottom maps are clear-sky area weighted average of AOD (AOD_{MODIS}^{clr}). Clear-sky weighted monthly mean AOD is derived by averaging daily mean aerosol optical depth weighted by daily $1^\circ \times 1^\circ$ gridded mean clear fraction where the clear fraction is derived from MODIS based cloud fraction on Terra and Aqua.

301

302

303

Figure 6 shows an hourly time series of AOD from MATCH, MERRA2 and AERONET for January 2010 at the Beijing China AERONET site. The top plot shows

304 cloud fraction time series derived from MODIS and GEOs from the SYN1deg Ed4.1
 305 product (Rutan et al. 2015), and the bottom plot shows AOD time series. Generally, both
 306 models produce a large variability of AOD at this site fairly well over the course of the
 307 month. While both MERRA2 and MATCH AODs increase near times when cloud
 308 fraction approaches 100%, the increase of MATCH AOD, which correlates with the
 309 increase of AERONET AOD relatively well, is larger than the increase of MERRA2
 310 AOD. Although the temporal correlation coefficient of the MATCH and AERONET
 311 AODs is smaller at this site during summer months than during winter months (not
 312 shown), a good temporal correlation between MATCH and AERONET AODs is
 313 consistent across most locations and times we considered. To show this statistically, in
 314 the following, we extend this analysis to a number of AERONET sites grouped
 315 geographically based on general aerosol type.
 316

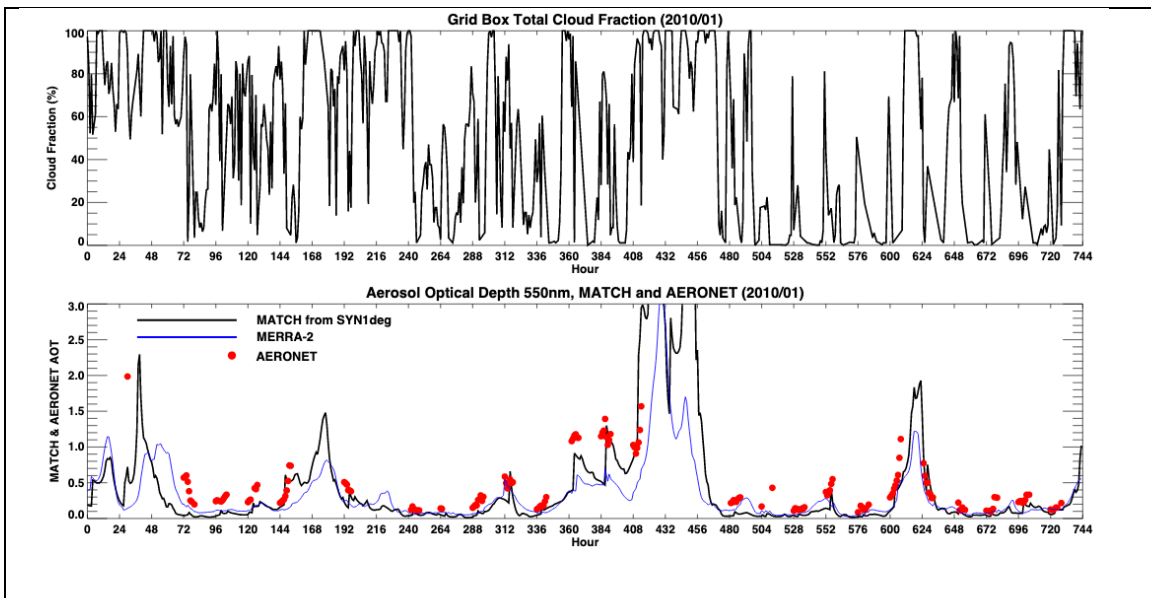
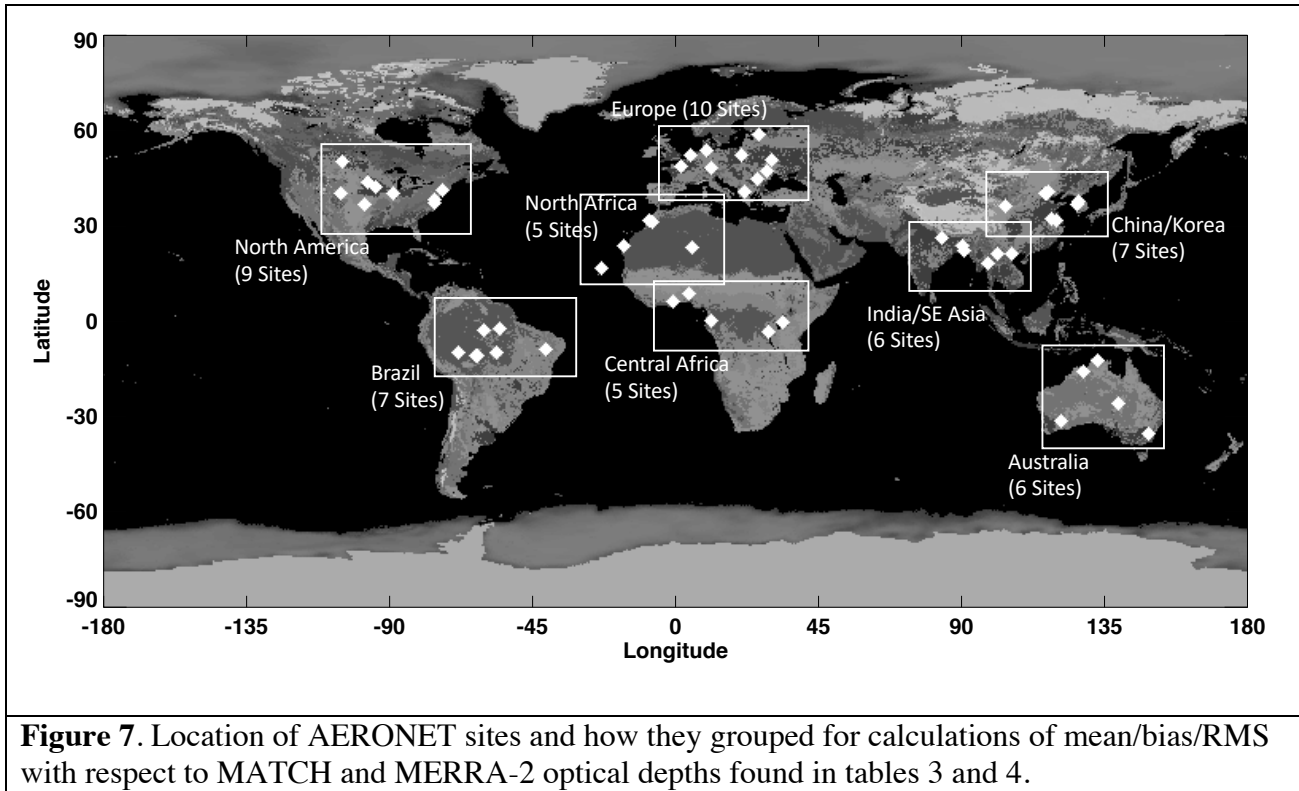


Figure 6. Hourly time series of grid box cloud fraction (top) from SYN1deg Ed4.1 CERES product and AOD (bottom). Results are from the grid box containing the AERONET Beijing, CH site. Black line MATCH, blue line MERRA-2, red dots, AERONET observations. MATCH and, to a lesser degree MERRA-2 often have large increases in AOD when cloud fraction nears 100%.

317

318 Aerosol optical depths from AERONET are nominally provided at 8 spectral
319 channels, every 20 minutes given favorable conditions. We use two channels to derive
320 observed AOD at 550 nm to compare to the AOD provided by the MATCH model.
321 Because the SYN1deg radiative transfer calculation is done hourly, we average any
322 observations within a given hour period centered at the 30th minute for each site
323 collocated within a SYN1deg grid box. AERONET sites chosen are shown in **Figure 7**
324 with a complete listing of all sites in Appendix 1. Though we examine 55 sites over 20+
325 years, we aggregate the statistics within continental regions which naturally isolates them
326 by general climatic conditions. Tables 3 and 4 show comparisons for each site grouping,
327 respectively, for clear sky (less than 1% cloud identified by MODIS and geostationary
328 satellites in the SYN1deg grid box) conditions and for all sky (any cloud condition within
329 the SYN1deg grid box) conditions. Using clear-sky scenes identified by MODIS only
330 gives the same statistical results with fewer number of samples. Statistics shown in
331 Tables 3 and 4 are the average observed value, mean bias (MATCH – Observation), root
332 mean square (RMS) difference and the correlation coefficient (R) over the time period
333 from March 2000 through February 2020. The actual time period varies depending on the
334 site due to AERONET data availability. The RMS difference and correlation coefficient
335 are computed by each site with hourly mean values where observations are available
336 from March 2000 through February 2020. For comparison purposes we show the same
337 statistics derived from observations compared to MERRA2 AODs using the identical
338 hours. We note, however, that MERRA2 assimilates AERONET while MATCH AODs
339 are independent from AERONET AODs. MATCH AOD for the Brazil group is biased

340 high by 0.02, and the China/Korea group has no appreciable bias compared with
 341 AERONET AODs. These two regions have relatively large bias of $\langle AOD_{MODIS}^{clr} \rangle$ from



342

343 MATCH compared with MODIS AODs (**Fig. 3** right). In contrast, negative bias of
 344 MERRA2 AODs compared with AERONET AODs for Brazil, central Africa, and
 345 China/Korea groups are consistent with negative bias of MERRA2 $\langle AOD_{MODIS}^{clr} \rangle$
 346 compared with MODIS AODs (**Fig. 3** left). For the China/Korea group, the RMS
 347 difference between MATCH AODs and AERONET AODs is 0.18 and correlation
 348 coefficient is 0.7. These are worse than the counterpart values of MERRA2 versus
 349 AERONET AODs because summertime agreement between MATCH and AERONET
 350 AODs is worse if a similar plot as **Fig. 6** is plotted for summertime when hygroscopic
 351 aerosols are dominant under high relative humidity conditions.

352 The sign of the MATCH AODs compared to AERONET AODs for all-sky
 353 conditions is generally consistent with the sign of clear-sky counterparts. The RMS
 354 difference under all-sky conditions is generally larger than the clear-sky RMS difference
 355 while the correlation coefficient is nearly the same. The biases for MERRA2
 356 comparisons are generally comparable to MATCH though RMS for MERRA2 tend to be
 357 slightly smaller and correlations tend to be higher due in part to the assimilation of
 358 AERONET into the MERRA2 model.
 359

Table 3. Hourly AERONET station statistics for MATCH and MERRA-2.
 Continental Groups, Clear Sky conditions¹

Site	MATCH						MERRA-2		
	Predominant Aerosol Type	Number	Observed Average	Bias	RMS	R ²	Bias	RMS	R ²
Australia (5 Sites)	Dust Smoke	20925	0.06	0.01	0.06	0.4	0.03	0.05	0.7
Brazil (7 Sites)	Smoke Polluted	6554	0.14	0.02	0.10	0.8	-0.02	0.08	0.9
Central Africa (5 Sites)	Smoke	2139	0.70	-0.10	0.24	0.9	-0.10	0.24	0.9
North Africa (5 Sites)	Dust	10047	0.17	0.07	0.15	0.7	0.02	0.10	0.8
China/Korea (8 Sites)	Polluted	2827	0.26	-0.00	0.18	0.7	-0.03	0.15	0.8
India/SE Asia (6 Sites)	Smoke Polluted	3010	0.51	-0.09	0.28	0.6	-0.10	0.24	0.8
North America (9 Sites)	Continental Polluted	21429	0.10	-0.00	0.07	0.7	0.00	0.06	0.8
Europe (10 Sites)	Continental Polluted	10211	0.13	0.01	0.07	0.7	-0.02	0.05	0.8

¹The time period used is from Mar 2000 through Apr 2020. Actual period varies by site depending on AERONET data availability. Clear Sky is identified by MODIS and geostationary satellites and the cloud fraction is less than 1% over a SYN1deg grid box.

360
 361 Results for all points across all sites and times are shown in **Figure 8**. The color density
 362 plots are in log scale and indicate the vast majority of observations have an AOD of less
 363 than one for both clear and all sky conditions observed within the SYN1deg grid box.

364 Biases are less than 10% of the mean value but RMS is large relative to the mean
 365 observed value. Overall correlation is approximately 0.8. The ‘clear sky’ hours (where
 366 SYN1deg estimated less than 1% cloud in the grid box based on MODIS and GEO
 367 observations) is a little more than 10% of the overall points. When MATCH AOD is
 368 compared to MERRA2 AOD (not shown) MATCH is biased approximately 10% higher.
 369

Table 4. Hourly AERONET station statistics for MATCH and MERRA-2.
 Continental Groups, All Sky Conditions¹

Site	Predominant Aerosol Type	Number	Observed Average	MATCH			MERRA-2		
				Bias	RMS	R ²	Bias	RMS	R ²
Australia (5 Sites)	Dust Smoke	110523	0.09	0.00	0.09	0.5	0.02	0.07	0.8
Brazil (7 Sites)	Smoke Polluted	72656	0.25	0.03	0.23	0.8	-0.04	0.18	0.9
Central Africa (5 Sites)	Smoke	41193	0.55	-0.07	0.26	0.8	-0.10	0.26	0.9
North Africa (5 Sites)	Dust	43205	0.23	0.08	0.20	0.7	0.01	0.14	0.8
China/Korea (8 Sites)	Polluted	52287	0.45	0.01	0.31	0.7	-0.08	0.27	0.8
India/SE Asia (6 Sites)	Smoke Polluted	44534	0.61	-0.06	0.32	0.6	-0.10	0.32	0.7
North America (9 Sites)	Continental Polluted	160356	0.13	0.02	0.13	0.6	0.00	0.09	0.7
Europe (10 Sites)	Continental Polluted	175010	0.18	0.04	0.14	0.6	-0.02	0.08	0.8

¹ The time period used for the statistics is from March 2000 through April 2020. Total sample varies by site depending on AERONET data availability.

370

371 **3. Discussion of AOD Differences**

372 In this section, we investigate the reason for the AOD differences shown in the
 373 previous section. In addition, we estimate the effect of the AOD differences to surface
 374 irradiances when MATCH AODs are used for surface irradiance computations.

375 Generally, cloud contamination in MODIS AODs is caused by unresolved sub-pixel scale
 376 clouds (Kaufman et al. 2005; Martins et al. 2002). The difference shown over convective
 377 regions, therefore, seems to be caused by the uncertainty due to 3D radiative effects that
 378 impact retrieved AODs by unknown amounts (Wen et al. 2007), by errors in estimating

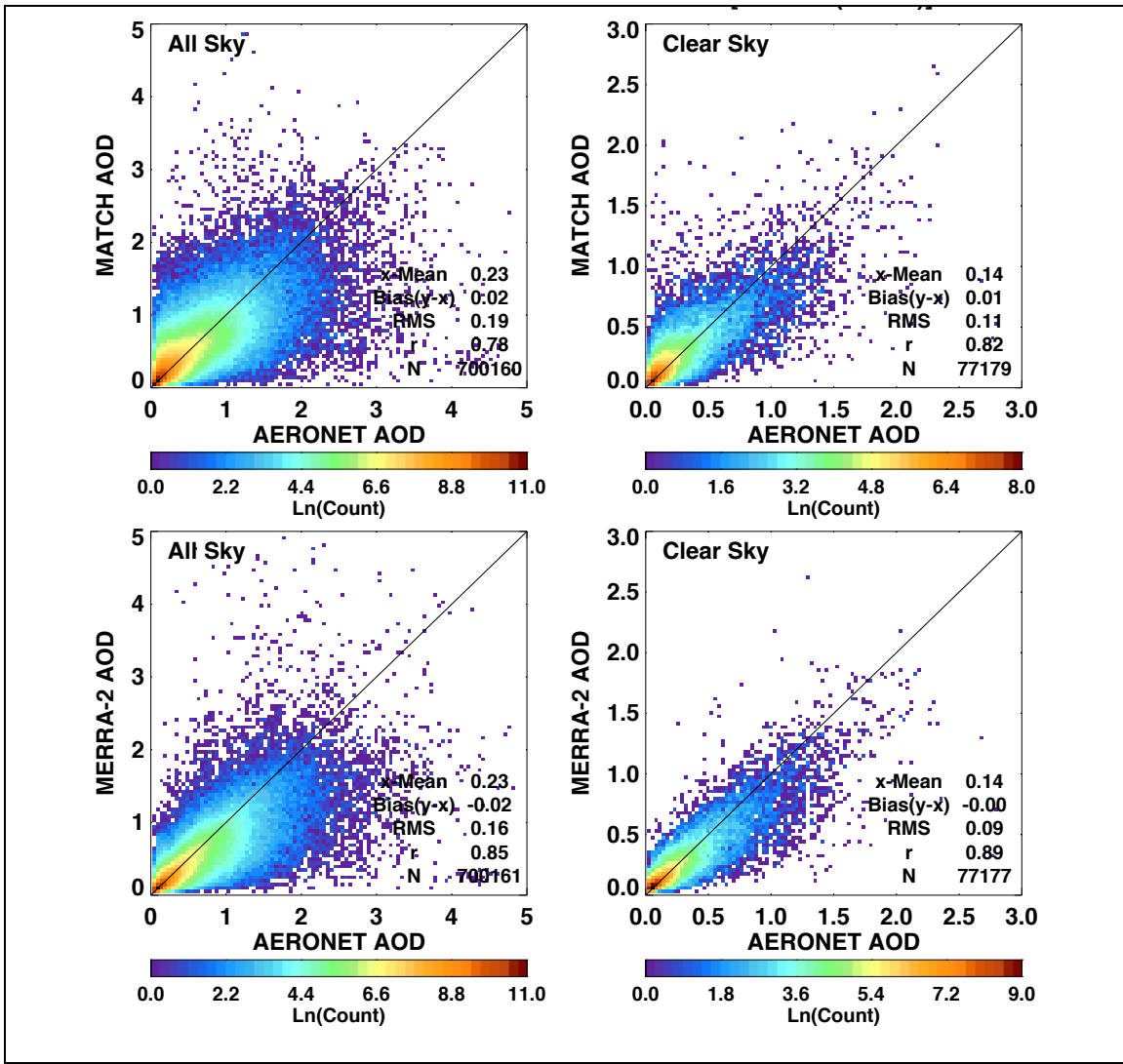


Figure 8. All sky (left) and clear sky (right) comparisons of observed (AERONET) hour mean optical depths to estimates from the MATCH model for 20+ years at 55 AERONET sites shown in Fig 7.

379
 380 the fraction of hygroscopic aerosols or by the errors in estimating water uptake by
 381 hygroscopic aerosols (Su et al 2008, Marshak et al., 2021). Larger AODs are screened out

382 in the MOD08 data product while the CERES team uses all retrieved AODs regardless of
383 the QAC score, likely increasing MATCH AOD overall. The comparison with
384 AERONET AODs is not decisive to determine how to screen MODIS AODs because
385 MATCH AODs are positively biased and MERRA2 AODs are negatively biased for the
386 Brazil group. The result underscores the difficulty of deriving accurate AODs, which
387 appear to involve requirements in addition to identification of clear-sky scenes. Levy et
388 al. (2013) list reasons lowering the QAC score as 1) pixels are thrown out due to cloud
389 masking, 2) retrieval solution does not fit the observation well, and 3) the solution is not
390 physically plausible given the observed situation. Therefore, even though the difficulty of
391 identifying clear-sky scenes is driven by cloud contamination by trade cumulus (Loeb et
392 al. 2018), the difficulty of deriving AODs exists over convective regions (Varnai et al.,
393 2017) as well.

394 Larger positive biases of MATCH AODs compared with AERONET AODs exist
395 over Africa (Tables 3 and 4). For North Africa, the bias is known to be caused by
396 excessive dust generated by the MATCH algorithm. Even though modeled aerosols are
397 not often used over north Africa owing to the abundance of clear-sky conditions, the dust
398 problem leads to a larger positive AOD bias. In addition, MATCH uses fixed aerosol
399 sources in time. Therefore, it tends to miss large aerosol events, such as forest fires, until
400 clear-sky conditions occur, allowing observations of the event by MODIS. This leads to a
401 larger RMS difference and lower correlation coefficient with AERONET AODs
402 compared with those from MERRA2 versus AERONET.

403 Because MODIS AOD are not generally available under overcast conditions, the
404 reliance on modeled AOD increases as the cloud fraction over a $1^\circ \times 1^\circ$ grid increases.

405 **Figure 6**, which shows that AERONET AOD increases with cloud fraction derived from
 406 satellites, indicates that as the cloud fraction over a $1^\circ \times 1^\circ$ grid increases, AOD over the
 407 clear-sky portion of the grid increases. In addition, **Fig. 6** suggests that modeled AODs
 408 under near overcast conditions are significantly larger than clear-sky AODs that are
 409 constrained by MODIS observations. Because we are unable to evaluate AODs for
 410 overcast conditions, here we assess AOD changes with cloud fraction using ground-based
 411 observations. **Figure 9** shows the distribution of AERONET AODs for clear-sky and all-
 412 sky conditions, as well as precipitable water derived from a microwave radiometer
 413 separated by these two conditions. Clear-sky is identified by the Long-Ackerman
 414 algorithm (Long et al. 2006) that uses surface direct and diffuse irradiances. **Figure 9**
 415 shows that AOD and precipitable water under all-sky conditions are significantly larger

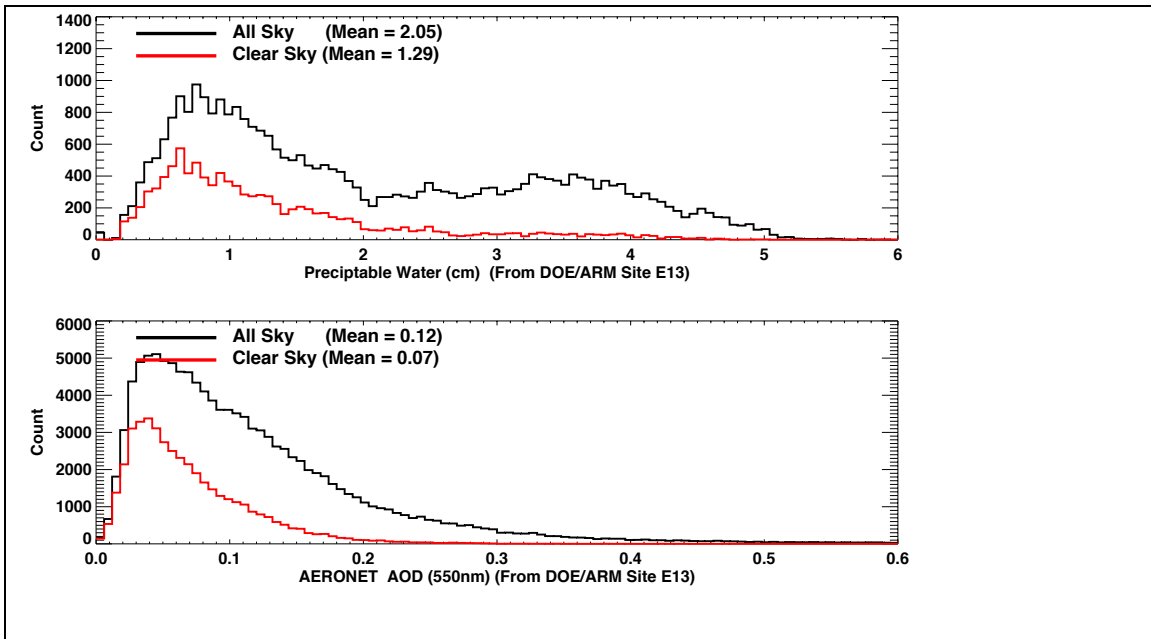


Figure 9. a) 15-minute mean precipitable water distributions from Microwave radiometer observations at ARM/SGP E13 site under all sky and clear sky conditions. b) 15-minute mean aerosol optical depth distributions from AERONET sun-photometer at 550nm. 'Clear sky' is here defined as when a 15-minute time period where the SWFA, surface radiometry-based cloud fraction, equals 0.

416

417 than those under clear-sky conditions. When we use cloud fraction derived from satellite
 418 and plot AOD and precipitable water as a function of the cloud fraction using the same
 419 grid box where the ground site is located, AOD and precipitable water increase with the
 420 cloud fraction (**Fig. 10**). Therefore, increasing AOD with cloud fraction shown in **Fig. 6**
 421 is qualitatively explained by increasing AOD of hygroscopic aerosols with relative
 422 humidity. However, **Fig. 10** indicates that either the growth of MATCH AOD is too
 423 strong or modeled MATCH AOD under all-sky conditions is too large.

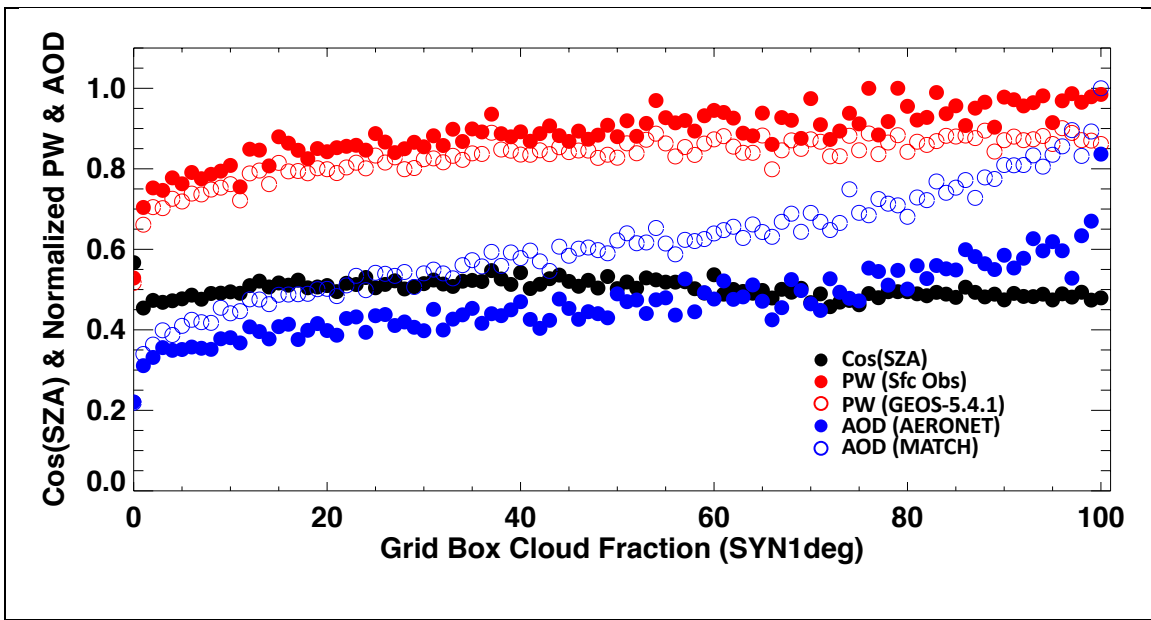


Figure 10. Aerosol optical depth (AOD) and precipitable water (PW) as a function of cloud fraction over the $1^{\circ} \times 1^{\circ}$ grid box where the ARM/SGP E13 and SURFRAD Bondville IL sites are located. Closed and open blue circles are, respectively, AOD derived from AERONET and MATCH AOD. Closed and open red circles are, respectively, PW derived from microwave radiometer and CIMEL sun photometer and GEOS-5.4.1 PW. Cloud fractions are derived from MODIS and geostationary satellites. Black dots are mean cosine solar zenith angle of the time of AOD and PW observations. AOD and PW are normalized to their maximum value for display.

424

425 **4. Clear Sky Comparisons of SYN1deg and Surface Observed Irradiances**

426 We consider the impact of MATCH aerosols on computed surface irradiances by
 427 comparing calculated hourly mean surface downward irradiances from the Ed4.1

428 SYN1deg-Hour product to observations of downward irradiance. In a $1^{\circ}\times 1^{\circ}$ grid box
429 with an approximate size of 111 km², 100% clear sky sampled over one hour as
430 determined by MODIS or geostationary satellites is relatively rare. None the less, by
431 grouping sites based on general surface conditions and analyzing 20 years of data
432 sufficient samples are found. **Figure 11** shows the sites, grouped by color, including 15
433 land sites labeled “Mid-Latitude” (Green), 6 sites labeled “Desert” (Red), 6 sites labeled
434 “Polar” (White) and 46 buoys (Blue). Surface observed SW irradiance from the land
435 sites comes from the Baseline Surface Radiation Network (Ohmura et al. 1998; Dreimel
436 et al. 2018) and buoy data are made available

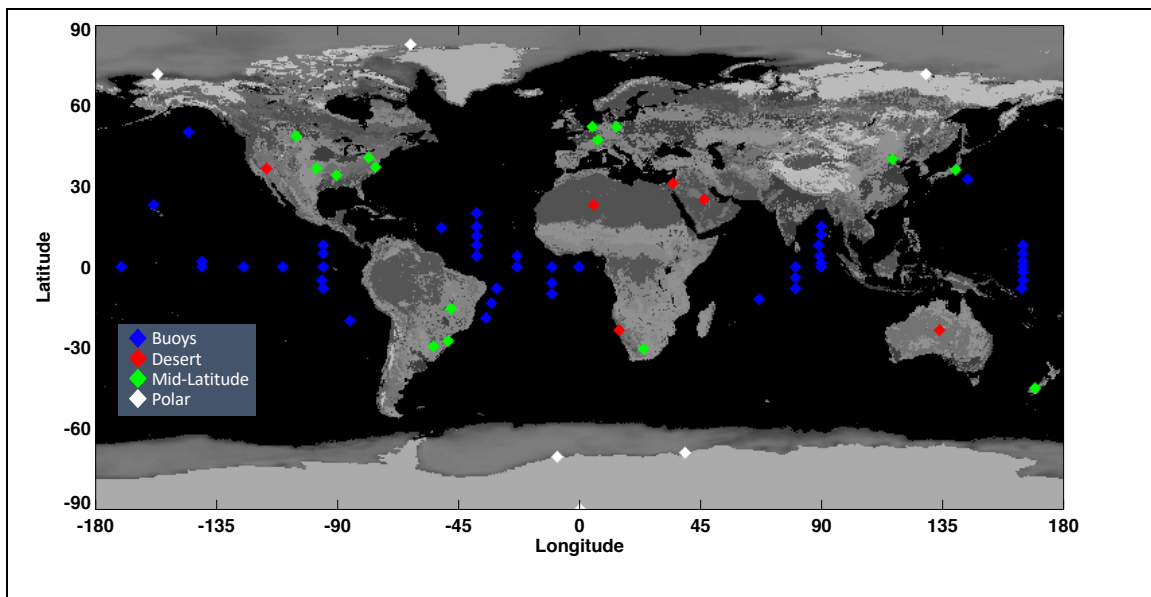


Figure 11. Location of surface observations of downwelling shortwave irradiance used to compare the SYN1deg Ed4.1 calculations to observations for all available hours (from Mar 2000 through Dec 2019) where the SYN1deg cloud analysis determines the hour and grid box to be 100% clear sky.

437
438 from the Pacific Marine Environmental Lab (PMEL) (McPhaden et al. 2002, 2009) and
439 the Woods Hole Oceanographic Institute (WHOI) (Colbo and Weller, 2009). A complete
440 listing is given in Appendix A.

441

4.1 Shortwave Comparisons

442

We begin with a simple sensitivity calculation of AOD on surface Downward

443

Shortwave Irradiance (DSI). **Figure 12** shows a series of radiative transfer calculations

444

using the “On-Line Langley Fu & Liou radiative transfer code

445

([https:// cloudsgate2.larc.nasa.gov/cgi-bin/fuliou/runfl.cgi](https://cloudsgate2.larc.nasa.gov/cgi-bin/fuliou/runfl.cgi)) with an open shrub spectral

446

albedo (broadband albedo of 0.14 at $\mu_0=1.0$), “continental” aerosol, and no clouds.

447

Values on the solid black line are calculated DSI with an AOD of 0.09 at six different

448

solar zenith angles. Calculations were then done for AODs of 0.0 and 0.18, at the same

449

solar zenith angles, representing 100% error bounds of mean AODs derived from

450

AERONET as found in Tables 3 and 4 for the Australia sites where the RMS is

451

approximately equal to the observed average of AOD. Orange and red shaded areas

452

indicate potential bias of DSI at a given solar zenith angle. Irradiance values scale nearly

453

linearly with $\text{Cos}(\text{SZA})$ between these limits. **Figure 12** shows the error remains nearly

454

constant until a $\mu_0=0.5$ where it begins to decrease as insolation decreases. However, due

455

to small downward irradiances at large solar zenith angles, the percentage error increases.

456

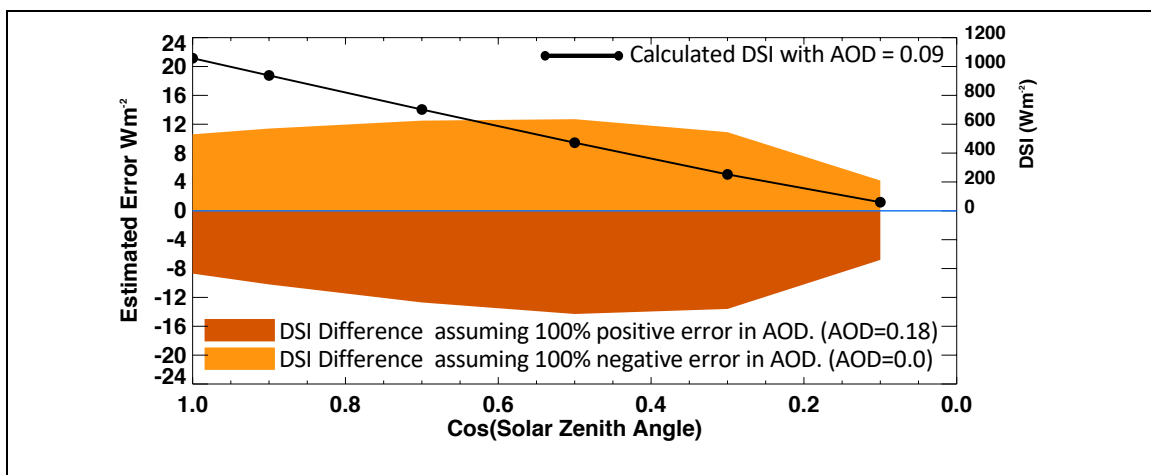


Figure 12. Calculated DSI error at the surface computed with the LFLRT model due to the error in AODs. AOD is assumed to be 0.09. Light and dark orange envelope indicate, respectively, positive and negative errors in Wm^{-2} (left axis) due to 100% AOD errors. Envelopes are computed with AODs of 0.0 (a -100% error) and 0.18 (a +100% error), at the same solar zenith angles, representing 100% error bounds. Values on the solid black line are calculated DSI (right axis) with an AOD = 0.09 at six solar zenith angles.

457

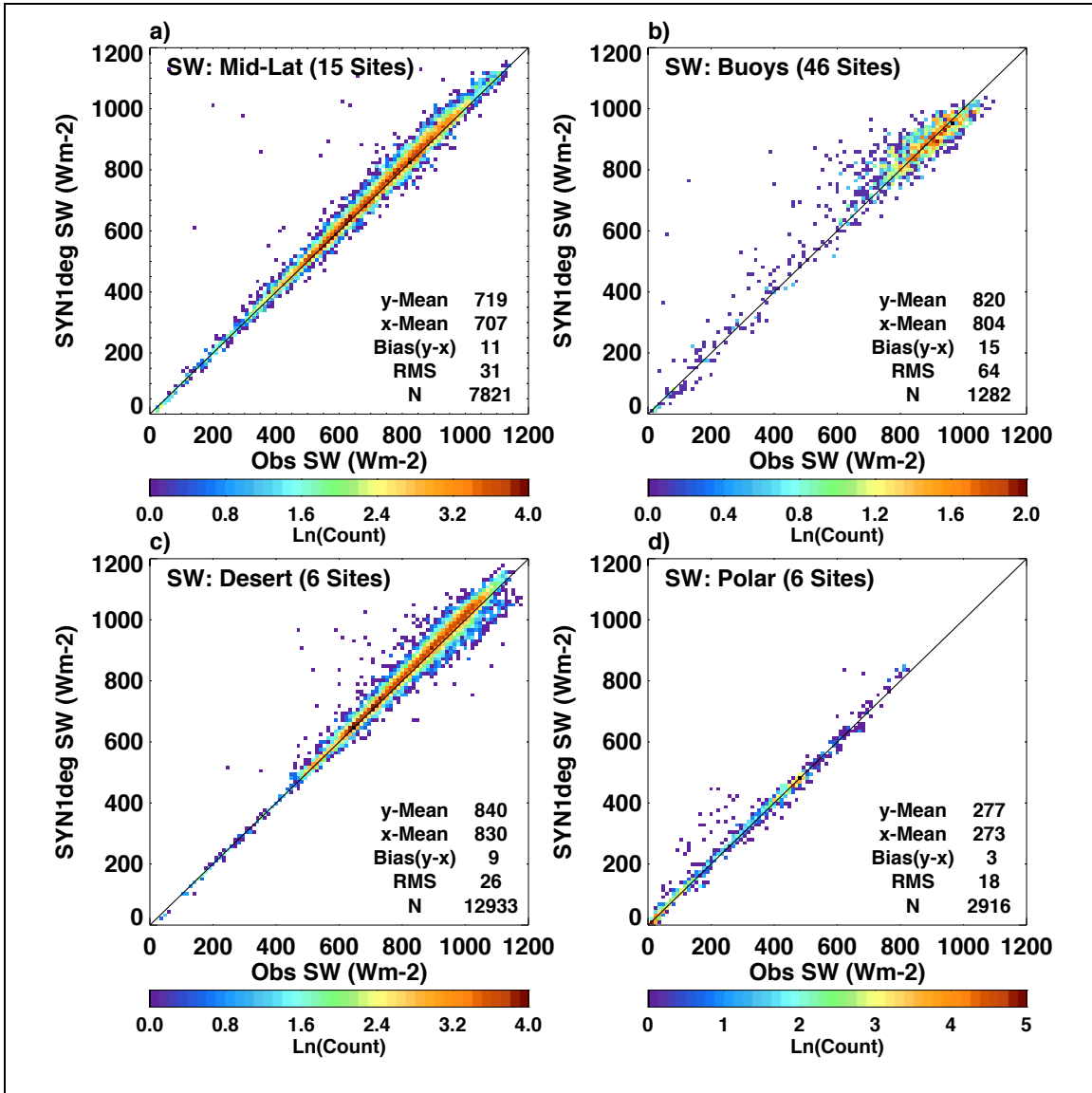


Figure 13. Comparisons of DSI at the surface from the SYN1deg Ed4.1 calculations (y-axis for all plots) and BSRN and buoy surface sites (x-axis all plots). Data are from Mar 2000 through Feb 2020 and only include hours when a 1° grid box is 100% clear sky according to SYN1deg cloud fraction.

458

459 **Figure 13** shows hourly comparisons of computed clear-sky downward
 460 shortwave irradiance compared to observations for the groups of sites shown in **Fig. 11**.
 461 In general, calculated irradiance is larger than observed. We find that in every grouping,
 462 SYN1deg calculations tend to be too transmissive, overestimating DSI by between 3
 463 Wm^{-2} (polar sites) and 15 Wm^{-2} (ocean buoys) with mid-latitude and desert sites each
 464 overestimating DSI by $\sim 10 \text{ Wm}^{-2}$. This points to the possibility that MATCH is weighted
 465 too far towards scattering aerosols and too few absorbing aerosols.

466 Clear-sky scenes used for **Fig. 13** are those identified by MODIS and
 467 geostationary satellites over the 1° grid box where the ground site is located. That is,
 468 when satellites did not detect clouds over the one-hour period within the grid box, we
 469 compared computed and observed hourly mean downward shortwave irradiances. DSI is
 470 nominally measured by a shaded pyranometer combined with the direct insolation
 471 measured by a pyrhelimeter on a solar tracker. Though satellites may indicate clear,
 472 clouds might have been present within the field-of-view of the pyranometer increasing
 473 diffuse radiation. This would increase observed DSI, hence modeled irradiance would be
 474 smaller. To verify, we used the ground-based cloud screening algorithm developed by
 475 Long and Ackerman (Long et al. 2006) to further screen clouds. For the land groupings,
 476 Table 5 shows bias (RMS) of the DSI where both satellite and surface based observed
 477 cloud fraction equal 0.0. Though mean bias did not change significantly, the RMS in both
 478 the Mid-Latitude and Desert sites was reduced by half due to the more stringent cloud
 479 screening.

Table 5. Bias (RMS) of clear sky surface shortwave calculation compared to observation¹.
 All in Wm^{-2}

<i>Cloud Analysis</i>	Mid Latitude	Desert	Polar
-----------------------	--------------	--------	-------

<i>Satellite</i>	11 (31)	9 (26)	3 (18)
<i>Satellite And Surface</i>	11 (16)	8 (15)	4 (19)

¹Sample is based on 20 years of calculations when either satellite or satellite and surface cloud analysis indicates 0% cloud.

480

481

4.2 Longwave Comparisons

482

In this section we consider the implications of errors in AOD and aerosol type on

483

longwave LFLRT calculations as found in the SYN1deg product. **Figure 14** shows

484

SYN1deg surface downward longwave irradiance (DLI) calculations compared to surface

485

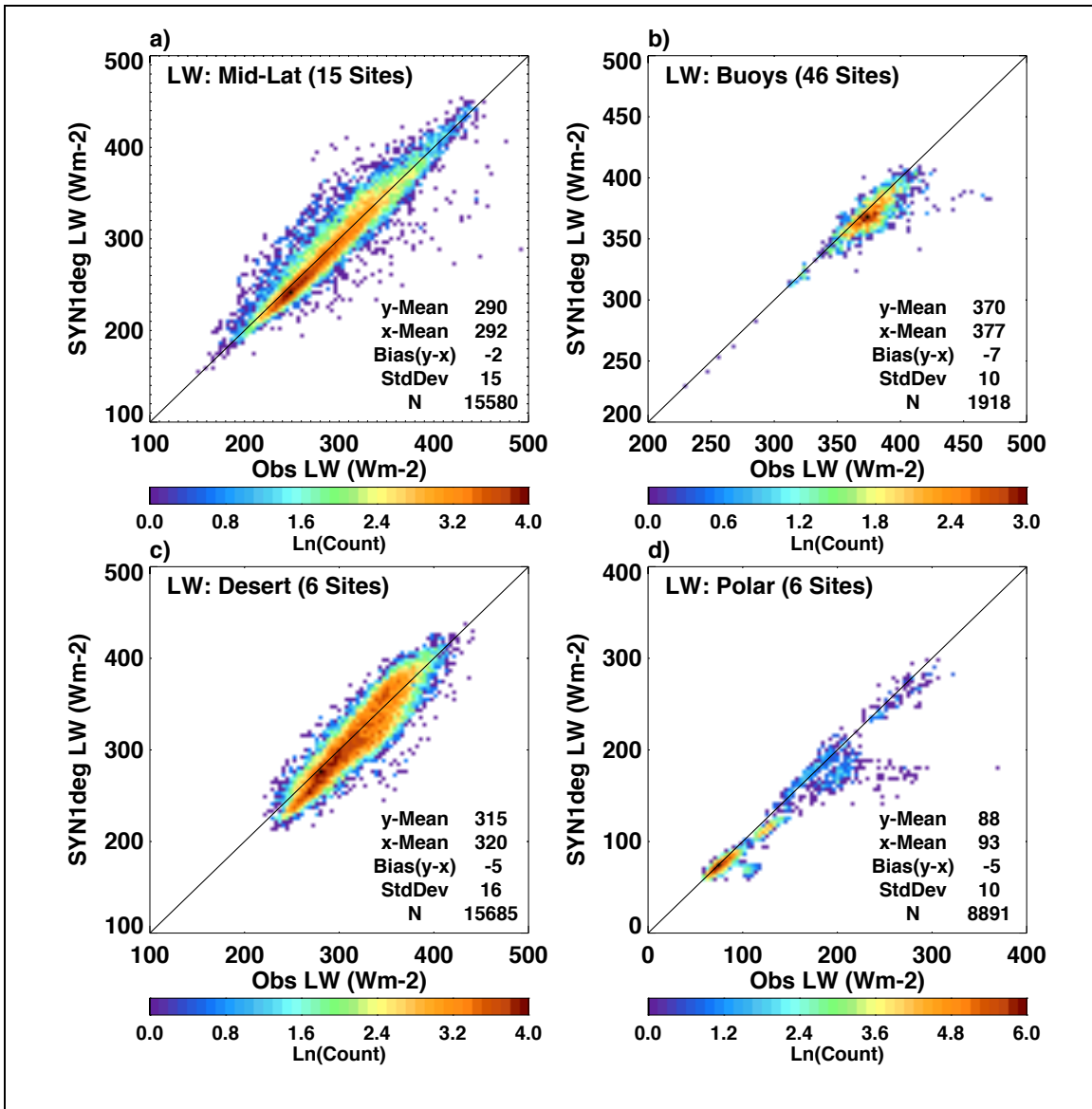


Figure 14. Comparisons of LW downward irradiance at the surface from the SYN1deg Ed4.1 calculations (y-axis for all plots) and BSRN and buoy surface sites (x-axis all plots). Data are from Mar 2000 through Feb 2020 and only include hours when a 1x1 grid box is 100% clear sky according to SYN1deg cloud fraction.

486

487 observations similar to those shown in **Fig. 13**. Except for the polar region, where DLI is
 488 very sensitive to near surface air temperature, the bias and standard deviations of the DLI
 489 is smaller than the SW equivalents in terms of both Wm^{-2} and percentage of the mean
 490 observation. Depending on aerosol type, DLI is less sensitive to total AOD. For example,
 491 a doubling of AOD (0.2 to 0.4) for a continental type results in a DLI change of only 0.2

492 W m⁻². Table 6, however, shows the sensitivity of DLI (and DSI) to changes in dust
 493 particle size and shows that for LW, a change in aerosol type results in up to a 10 Wm⁻²
 494 change in DLI.

Table 6. Effect of Dust Particle size on Surface Irradiance Calculations¹

	Dust Particle Size (microns)		
	0.5	2.0	8.0
<i>DLI</i>	352 Wm ⁻²	359 Wm ⁻² (+2.0%)	362 Wm ⁻² (+2.8%)
<i>DSI</i>	1046 Wm ⁻²	1032.8 Wm ⁻² (-1.7%)	1020 Wm ⁻² (-2.5%)

¹The radiative transfer code is run for a Mid-Latitude Summer atmosphere, open shrub surface albedo, aerosol scale height of 1.5km, clear sky, and cosine solar zenith angle of 1.0. Aerosol optical depth is fixed at 0.2 for all calculations.

495
 496 DLI is thus more sensitive to aerosol type in certain regions of the globe where there is
 497 substantial dust. To see the potential impact on DLI **Figure 15** shows calculated LW
 498 downward radiative forcing (clear minus pristine calculations) at 57 AERONET sites
 499 across the 20 years of SYN1deg data under consideration. The Northwest Africa sites
 500 (where dust is found seasonally) are shown as red boxes where one clearly sees larger
 501 LW forcing at these sites. Given the importance of particle size to LW effect we check
 502 MATCH particle size against AERONET fine/coarse mode retrievals for several of the
 503 African AERONET sites. **Figure 16** plots canonical mean observations of fine and coarse
 504 mode AOD from three AERONET sites along with groupings of AOD species from the
 505 MATCH model output. To compare to AERONET fine mode observations we plot the
 506 sum of the MATCH AOD due to organic carbon (OC), black carbon (BC) and sulfate
 507 (SO₄). We compare the sum of MATCH AOD large dust particles (> 1µm) along with
 508 sea salt (though sea salt is essentially zero over land) to the coarse mode AERONET
 509 optical depth. All AOD values are at 550nm.

510

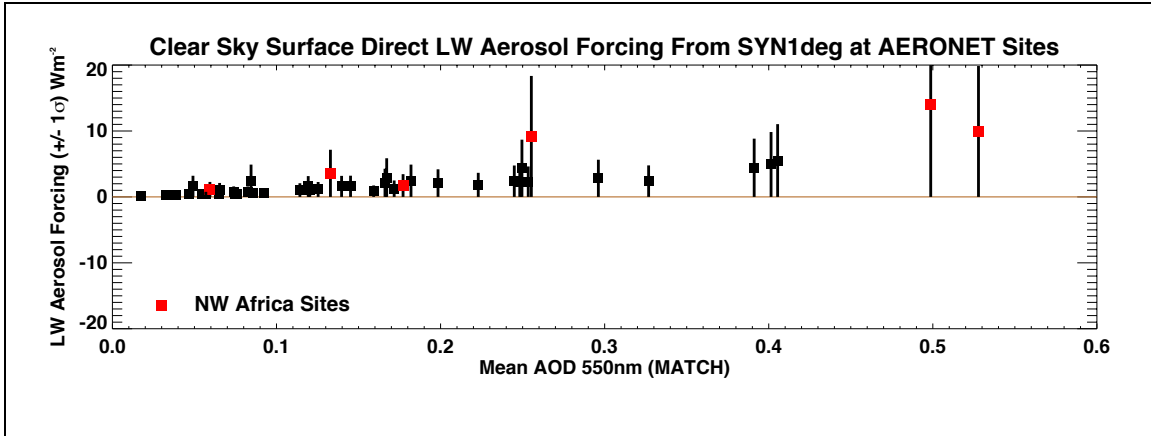


Figure 15. Clear sky direct radiative effect (clear minus pristine) in downward longwave irradiance averaged from 2000 through 2020 when AERONET observations are available. Boxes indicate average, vertical bar is +/- one standard deviation. Black boxes indicate all 57 AERONET sites and red boxes indicate Northwest Africa sites.

511

512 **Figure 16** indicates that resultant fine/coarse mode comparisons are encouraging but the
513 agreement is site dependent. In general MATCH is capturing seasonal changes in fine
514 and coarse particles at these sites but the magnitude of the AODs is biased.

515

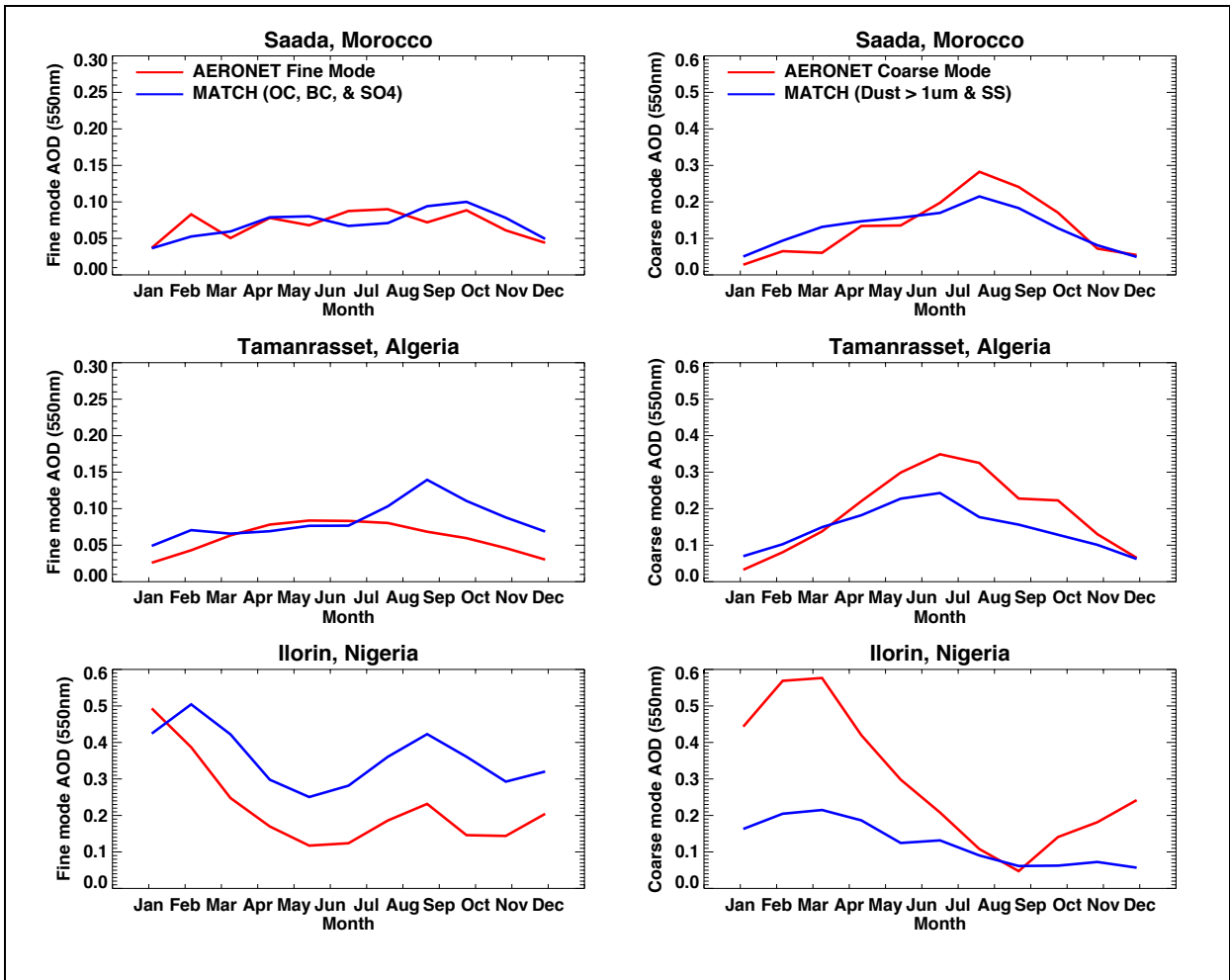


Figure 16. Canonical monthly means across 20 years (2000-2020) showing AERONET fine (left) and coarse (right) AOD at 550nm compared to MATCH constituents. MATCH values represent summations of organic, black carbon (OC, BC) and sulfate (SO₄) for fine mode and large dust particles (> 1micron) plus sea salt for coarse mode comparisons.

516

517

4.3 CERES TOA and EBAF-surface comparison

518

CERES instruments observe TOA irradiances, which can be used to assess the

519

bias in computed irradiance. Global annual mean clear-sky TOA irradiances derived from

520

CERES observation averaged over 20 years from March 2000 through February 2020 are

521

53 Wm⁻² for reflected shortwave irradiance and 268 Wm⁻² for emitted longwave

522

irradiance. Corresponding computed reflected shortwave flux is 51 Wm⁻² and emitted

523

longwave flux is 267 Wm⁻². Insight into the surface irradiance errors may be gained by

524 considering how surface irradiance is modified via the tuning algorithm to match TOA
525 irradiance in the CERES EBAF-surface product (Kato et al. 2018). After known biases
526 are taken out, the adjustment of temperature and specific humidity profiles, surface and
527 aerosol properties are derived based on their pre-assigned uncertainty and the difference
528 of computed and observed TOA shortwave and longwave irradiance using the Lagrange
529 multiplier approach. To match the computed shortwave and longwave fluxes, AOD is
530 increased from 0.136 to 0.156 (global annual mean values) and precipitable water is
531 decreased from 2.29 cm to 2.22 cm (global annual mean values). These adjustments
532 change the downward shortwave irradiance from 244 Wm^{-2} to 243 Wm^{-2} .

533 To analyze how the EBAF tuning process changes surface irradiance, AOD and
534 precipitable water, we computed the mean change separated by surface group shown in
535 **Fig 11**. Generally, AOD increases and precipitable water decreases to increase reflected
536 shortwave flux, which in turn decreases surface downward shortwave irradiance over
537 these regions (**Table 6**). For the midlatitude group, on average, AOD is increased by
538 0.02, precipitable water is decreased by 0.06 cm, and surface albedo is increased by 0.03.
539 These adjustments reduce the diurnally averaged downward shortwave irradiance at the
540 surface by 2 Wm^{-2} . We do not have exact matches of BSRN and AERONET surface sites
541 but Tables 3 and 4 show MATCH AODs have either no bias (north America and China
542 and southeast Asia) or slightly negatively biased by 0.01 (Europe). Therefore, increasing
543 MATCH AODs by 0.02 on average for the mid-latitude group seems justifiable.
544 However, decreasing 2 Wm^{-2} for the diurnally averaged downward shortwave is smaller
545 than the 11 Wm^{-2} bias shown in the top left plot of **Fig. 13**, although instantaneous
546 irradiances are used for **Fig. 13**. The positive bias found in the downward shortwave

547 irradiance for the North Africa group (**Fig 13c**) is not consistent with the positive bias of
548 aerosol optical depth shown in **Table 3** under clear-sky conditions.

549 The adjustment made to match TOA shortwave irradiance, in the EBAF product,
550 is within the uncertainty of MODIS-derived AOD of ± 0.05 over land and ± 0.03 over
551 ocean (Remer et al. 2008; Levy et al. 2010, 2013). However, these are an expected error
552 of instantaneous AOD retrieval derived from the comparison of AODs with AERONET.
553 Therefore, the bias averaged over ground sites and many years is expected to be much
554 smaller. Although, the 0.03 AOD adjustment over ocean might be the upper limit of the
555 uncertainty of MODIS AODs over ocean, 16 Wm^{-2} bias in the instantaneous downward
556 shortwave irradiance seems to be larger than the reduction by 2 Wm^{-2} in the diurnally
557 averaged downward shortwave irradiance.

558 While we cannot identify the cause of the discrepancy between AOD comparison
559 and downward shortwave irradiance comparison with surface observations, potential
560 issues are following. 1) Aerosol type and optical properties used in irradiance
561 computations, and 2) bias in downward shortwave irradiance measured by pyranometer,
562 especially diffuse irradiance at smaller solar zenith angles. Because of the temperature
563 gradient within pyranometer, the downward shortwave irradiance measured by a
564 pyranometer tends to be biased low under clear-sky condition (Haeffelin et al. 2001).
565 Note that a study by Ham et al. (2020) indicates that the bias of diurnally averaged
566 surface downward shortwave irradiance computed by a four-stream model should be
567 smaller than 1%.

568

569

Table 6: Radiative flux, aerosol optical depth (AOD), precipitable water, and surface albedo change to match observed top-of-atmosphere radiative fluxes

Site	Observed TOA upward shortwave irradiance (Wm ⁻²)	Changes: Adjusted - Unadjusted				
		Clear-sky TOA upward shortwave irradiance (Wm ⁻²)	Clear-sky surface downward shortwave irradiance (Wm ⁻²)	Clear-sky AOD	Clear-sky precipitable water (cm)	Clear-sky surface albedo
<i>Mid-Latitude</i>	63.3	3.9	-2.0	0.02	-0.06	0.03
<i>Desert</i>	92.3	3.4	-1.7	0.02	-0.04	0.01
<i>Polar</i>	86.5	8.2	-0.2	0.01	-0.03	0.10
<i>Buoys</i>	42.0	1.6	-2.0	0.03	-0.12	0.00

570

571 **5. Conclusions**

572 We evaluated MATCH aerosol optical depth used to produce the CERES
573 SYN1deg product. Aerosol optical depths derived from Terra and Aqua by the dark target
574 and deep blue algorithms were merged to produce daily gridded AODs. Daily gridded
575 AODs were used for assimilation by MATCH at local solar noon. As a consequence,
576 monthly mean AODs under clear-sky conditions identified by MODIS closely agree with
577 those derived from MODIS, although MATCH uses climatological aerosol sources.
578 Because AODs are not screened by QAC, MATCH AODs are larger over convective
579 regions (e.g. Amazon, central Africa, and south east Asia) for both clear-sky and all-sky
580 conditions.

581 MATCH AODs under all-sky conditions are larger than those under clear-sky
582 conditions. Time series of AERONET AODs indicate that AODs generally increase with
583 cloud fraction, which is consistent with, primarily, water uptake by hygroscopic aerosols
584 (Varnai et al, 2017). In addition, surface observations at the ARM SGP site suggest that a
585 larger AODs and larger precipitable water under all-sky conditions than those under

586 clear-sky conditions. Aerosol optical depth biases from AERONET AODs are
587 comparable to biases of MERRA2 AOD biases from AERONET AODs for both all-sky
588 and clear-sky conditions. However, MERRA2, which uses AERONET AODs to train the
589 algorithm, has better temporal correlation with AERONET AODs than MATCH AODs.

590 Once MATCH AODs are used for surface irradiance computations, downward
591 shortwave irradiances are positively biased by 1% to 2% compared to those observed at
592 surface sites. Top-of-atmosphere reflected clear-sky shortwave irradiances are negatively
593 biased compared with those derived from CERES observations. Increasing AODs by
594 ~ 0.02 , and surface albedos by 0.03, and decreasing precipitable water by 0.06 cm over
595 mid-latitude surface sites makes computed reflected TOA irradiances agree with those
596 derived from CERES. These adjustments reduce downward shortwave irradiances at the
597 surface by 2 Wm^{-2} . Decreasing MATCH AODs for the desert group is needed to match
598 computed reflected shortwave irradiances at TOA with those derived from CERES.
599 However, decreasing MATCH AODs is not consistent with generally larger MATCH
600 AODs compared with AERONET.

601 Optical properties of aerosols (i.e. aerosol type) play a role in computing
602 shortwave and longwave irradiance and changing and/or incorrect aerosol type can alter
603 the downward irradiances. Aerosol types used in the computations rely on the mapping of
604 MATCH types to those available in the radiative transfer model (Table 2). Biases in the
605 fraction of each aerosol type and their optical properties can change TOA upward and
606 surface downward shortwave irradiances without altering total AOD. A fuller evaluation
607 of aerosol type is left for future study.

608

609 **Acknowledgments**

610 This work was funded by the NASA CERES project. The products and the
611 validation could not have been accomplished without the help of the CERES TISA team.
612 These data were obtained from the NASA Langley Research Center EOSDIS Distributed
613 Active Archive Center. We also wish to acknowledge the hard work put in by the many
614 dedicated scientists maintaining surface instrumentation in many diverse climates to
615 obtain high quality observations of downwelling shortwave and longwave surface flux.

616 Those groups are noted in Appendix A. We would also like to thank the anonymous
617 reviewers for their in-depth reading and assessment of the paper which led to significant
618 improvements in the manuscript.

619

620

621

622

623

624

625

626

627

628

629

630

631

632
 633
 634
 635
 636
 637
 638
 639
 640
 641
 642

Appendix A. Surface Observation Sites Used for Validation

A great deal of data used in this study was collected by dedicated site scientists measuring critical climate variables around the world. The tables included in this appendix outline the sites, in situ measurements taken and their locations and dates of available data. Table A1 lists the locations of the AERONET sites, our source for observed aerosol optical depth which can be found on-line at: https://aeronet.gsfc.nasa.gov/new_web/index.html.

Table A1. AERONET Observation Sites

Region	Site	Location	Available Months
North Africa (5 Sites)	Saada, Morocco	31.6N, 8.2W	2004/07 - 2019/04
	Ouarzazate, Morocco	30.9N, 6.9W	2012/02 - 2015/06
	Dhaka, Morocco	23.7N, 15.9W	2002/02 - 2005/11
	Tamanrasset, Algeria	22.8N, 8.2E	2004/07 - 2019/04
	Cape Verde Island	16.7N, 22.9W	2000/03 - 2018/12
Central Africa (5 Sites)	Ilorin, Nigeria	8.5N, 4.7E	2000/03 - 2019/09
	Koforidua, Ghana	6.1N, 0.3W	2012/12 - 2019/04
	Lope, Gabon	0.2S, 11.6E	2014/04 - 2018/02
	Mbita, Kenya	0.4S, 34.2E	2006/03 - 2017/17
	Bujumbura, Burundi	3.4S, 29.4E	2013/12 - 2019/04
China, Korea (8 Sites)	Xinglong, China	40.4N, 117.6E	2006/02 - 2014/11
	Beijing, China	39.9N, 116.4E	2001/03 - 2019/03
	Anymon Isl, S Korea	36.5N, 126.3E	2000/03 - 2019/11
	Yonsei Univ, S Korea	37.6N, 126.9E	2011/03 - 2019/01
	Cuiying Mt, China	35.9N, 104.1E	2006/07 - 2013/05
	Nanjing, China	32.2N, 118.7E	2008/03 - 2010/04
	Taihu, China	31.4N, 120.2E	2005/09 - 2016/08
	XiangHe, China	39.7N, 116.9E	2001/03 - 2017/05
India, SE Asia (8 Sites)	Gandhi College, India	25.8N, 84.1E	2006/04 - 2019/11
	Luang Namtha, Laos	20.9N, 101.4E	2001/04 - 2019/02
	Omkoj, Thailand	17.8N, 98.4E	2003/02 - 2018/03
	Dhaka Univ, Bangladesh	23.7N, 90.3E	2012/06 - 2019/07
	Bhola, Bangladesh	22.2N, 90.7E	2013/04 - 2019/04
	Nghia Do, Vietnam	21.0N, 105.8E	2010/11 - 2019/09
	Pune, India	18.5N, 73.8E	2004/10 - 2019/06
	Hanimaadhoo, Maldives	6.7N, 73.2E	2004/11 - 2019/09

643
 644

645
646
647
648

Table A1. AERONET Observation Sites (Continued)

Region	Site	Location	Available Months
Brazil (7 Sites)	Petrolina, Brazil	9.1S, 40.4W	2004/07 - 2016/11
	Abracos Hill, Brazil	10.7S, 62.4W	2000/03 - 2005/10
	Alta Floresta, Brazil	9.9S, 56.1W	2000/05 - 2019/02
	Belterra, Brazil	2.6S, 55.0W	2000/03 - 2005/04
	Ji Parana SE, Brazil	10.9S, 61.9W	2006/01 - 2017/10
	Manaus, Brazil	2.9S, 60.0W	2011/02 - 2019/05
	Rio Branco, Brazil	9.9S, 67.9W	2000/07 - 2017/10
Australia (6 Sites)	Jabiru, Australia	12.6S, 132.9E	2000/03 - 2019/09
	Lake Argyle, Australia	16.1S, 128.7E	2001/10 - 2019/09
	Canberra, Australia	35.3S, 149.1E	2003/01 - 2017/08
	Birdsville, Australia	25.9S, 139.3E	2005/08 - 2018/06
	Lucinda, Australia	18.5S, 146.4E	2009/10 - 2020/01
	Lake Lefroy, Australia	31.2S, 121.7E	2012/06 - 2019/12
North America (10 Sites)	Brats Lake, Canada	50.2N, 104.7W	2000/03 - 2013/02
	Sioux Falls, SD	43.7N, 96.6W	2001/06 - 2017/10
	Ames, IA	42.0N, 93.8W	2004/05 - 2019/03
	Boulder Tower	40.0N, 105W	2001/05 - 2016/07
	Bondville, IL	40.0N, 88.4W	2000/03 - 2017/10
	Brookhaven, NY	40.8N, 72.9W	2002/09 - 2020/01
	Wallops Island, VA	37.9N, 75.5W	2003/03 - 2020/03
	ARM/SGP E13	36.6N, 97.5W	2000/03 - 2018/05
	Chesapeake Light Tower	36.9N, 75.7W	2000/03 - 2016/01
	Table Mountain, CO	40.1N, 105.2W	2008/11 - 2017/12
Europe (10 Sites)	Cabauw, Netherlands	51.9N, 4.9E	2003/04 - 2017/11
	Palaiseau, France	48.7N, 2.2E	2000/03 - 2020/10
	Torevere, Estonia	58.2N, 26.5E	2002/06 - 2019/07
	Kishinev, Moldova	47.0N, 28.8E	2000/03 - 2018/11
	Belsk, Poland	51.8N, 20.8E	2004/01 - 2016/08
	Kyiv, Ukraine	50.3N, 30.5E	2007/04 - 2018/12
	Hamburg, Germany	53.5N, 9.9E	2000/06 - 2018/06
	Munich Univ, Germany	48.1N, 11.6E	2001/11 - 2019/05
	Thessaloniki, Greece	40.6N, 22.1E	2003/06 - 2020/03
	Bucharest, Hungary	44.3N, 26.0E	2000/10 - 2019/03

649

650 Sources of surface observed downwelling irradiance are outlined in Tables
651 A2 (land) and A3 (buoys). For land we utilize data from the Baseline Surface
652 Radiation Network (BSRN) (Dreimel et al, 2018; Ohmura et al. (1998)), the US Dept.
653 of Energy's Atmospheric Radiation Measurement (ARM) program and NOAA's
654 SURFRAD network available from NOAA's Air Resources Laboratory/Surface
655 Radiation Research Branch., Augustine et al. (2000). Buoy observations come from

656 two sources through four separate projects. The Upper Ocean Processes group at
657 Woods Hole Oceanographic Institute have maintained the Stratus, North Tropical
658 Atlantic Site (NTAS) and Hawaii Ocean Time Series (HOTS) buoys for more than a
659 decade providing valuable time series of radiation observations in climatically
660 important regions of the ocean. These data can be retrieved from:
661 <http://uop.whoi.edu/index.html>. We would also like to acknowledge the Project
662 Office of NOAA's Pacific Marine Environmental Labs (PMEL) where three groups of
663 buoy data were downloaded: In the Pacific, the Tropical Atmosphere
664 Ocean/Triangle Trans-Ocean Buoy Network (TAO/TRITON) (McPhaden, 2002) data,
665 from the tropical Atlantic Ocean, the Prediction and Research Moored Array in the
666 Tropical Atlantic (PIRATA) (Servain et al. 1998), and the Research Moored Array for
667 African - Asian - Australian Monsoon Analysis and Prediction (RAMA) (McPhaden et
668 al., 2009) in the Indian Ocean. Also downloaded from PMEL are the long-term buoy
669 observations PAPA and Kuroshio Current observatory sites.

670

671

672

673

674

675

676

677

678

679

680

Table A2. Surface Irradiance Validation Sites (Land)

Region	Site	Location	Source
Mid-Latitude (15 Sites)	Lindenberg, Germany	52.2N, 14.1E	BSRN
	Cabauw, Netherlands	51.9N, 4.9E	BSRN
	Fort Peck, MT	48.3N, 105.1W	BSRN
	Payerne, Switzerland	46.8N, 6.9E	BSRN
	Penn State, PA	40.7N, 77.9W	SURFRAD
	Beijing, China	39.9N, 116.3E	BSRN
	E13, Lamont, OK	36.6N, 97.5W	ARM
	Ches Light Tower, USA	36.9N, 75.7W	BSRN
	Tateno, Japan	36.1N, 140.1E	BSRN
	Goodwin Creek, MS	34.2N, 89.9W	SURFRAD
	De Aar, South Africa	30.6S, 24.0E	BSRN
	Lauder, New Zealand	45.0S, 169.7E	BSRN
	Florianapolis, Brazil	27.5S, 48.5W	BSRN
	Brasilia, Brazil	15.6S, 47.7W	BSRN
	Sao Martinho da Serra, Brazil	29.4S, 53.8W	BSRN
Desert (6 Sites)	Sede Boqer, Israel	30.8N, 34.7E	BSRN
	Saudi Solar Village	24.9N, 46.4E	BSRN
	Tamanrasset, Algeria	22.8N, 5.5E	BSRN
	Desert Rock, NV	36.6N, 116.1W	SURFRAD
	Alice Springs, Australia	23.7S, 133.8E	BSRN
	Gobabeb, Namibia	23.5S, 15.0E	BSRN
Polar (6 Sites)	Alert, Canada	82.5N, 62.4W	BSRN
	Tiksi, Russia	71.6N, 128.9E	BSRN
	Barrow, Alaska	71.3N, 156.7W	BSRN
	Syowa, Antarctica	69.0S, 39.5E	BSRN
	South Pole, Antarctica	90.0S, 0.5E	BSRN
	G. von Neumayer, Antarctica	-70.6S, 8.3W	BSRN

BSRN: Baseline Surface Radiation Network, <http://bsrn.awi.de/>SURFRAD: NOAA- SURFace RADiation Program, <http://www.esrl.noaa.gov/gmd/grad/surfrad/>ARM: US Dept of Energy, Atmospheric Radiation Measurement Program, <http://www.arm.gov/>

681

682

683

684

Table A3. Surface Observation Sites for Ocean Buoy Locations

Program Name	Data Source	Locations
Upper Ocean Processes Group (UOP) 3 Buoys	Woods Hole Oceanographic Institute	Stratus Buoy -20.2N, 85.0W
		North Tropical Atlantic Buoy 14.5N, 51.0W
		Hawaii Ocean Time Series Buoy 22.5N, 158W
PIRATA Buoys 14 Buoys	Pacific Marine Environmental Laboratory (PMEL)	East Atlantic Ocean
RAMA Buoys 10 Buoys	PMEL	Tropical Indian Ocean
TAO Array Buoys 17 Buoys	PMEL	E & W Tropical Pacific Ocean
Kuroshio Extension Observatory Buoy	PMEL	NW Pacific, 32.4N, 144.6E
PAPA Sub-Arctic Ocean Buoy	PMEL	NE Pacific, 50.1N, 144.8W

UOP: <http://uop.whoi.edu/projects/projects.htm>PMEL: http://www.pmel.noaa.gov/tao/data_deliv/deliv.html

685

686

687

688

689 **References**

690 Augustine, J. A., DeLuisi, J. J., and Long, C. N.: SURFRAD – A national surface radiation
691 budget network for atmospheric research, Bull. of Amer. Met. Soc. 81, No. 10, pp.
692 2341-2358, 2000.

693 Barth, M. C., Rasch, P. J., Kiehl, J. T., Benkovitz, C. M., and Schwartz, S. E.: Sulfur
694 chemistry in the NCAR CCM: Description, evaluation, features and sensitivity to
695 aqueous chemistry, J. Geophys. Res., 106, 20 311–20 322, 2000.

696 Bauer, S. E. and Menon, S.: Aerosol direct, indirect, semidirect, and surface albedo
697 effects from sector contributions based on the IPCC AR5 emissions for
698 preindustrial and present-day conditions, J. Geophys. Res., 117, D01206,
699 doi:10.1029/2011JD016816, 2012.

700 Benkovitz, C. M., Scholtz, M. T., Pacyna, J., Tarrason, L., Dignon, J., Voldner, E. C., Spiro,
701 P. A., Logan, J. A., and Graedel, T. E.: Global gridded inventories of anthropogenic
702 emissions of sulfur and nitrogen, J. Geophys. Res.: Atmos. 101 (D22), 29,239–
703 29,253, 1996.

704 Blanchard, D. C. and Woodcock, A. H.: The production, concentration and vertical
705 distribution of the sea-salt aerosol, Ann. Of the NY Acad. Of Sci.,
706 doi:10.1111/j.1749-6632.1980.tb17130, 1980.

707 Boucher, O., Randall, D., Artaxo, P., Bretherton, C., Feingold, G., Forster, P., Kerminen,
708 V.-M., Kondo, Y., Liao, H., Lohmann, U., Rasch, P., Satheesh, S.K., Sherwood, S.,
709 Stevens, B. and Zhang, X. Y.: Clouds and Aerosols. In: Climate Change 2013: The

710 Physical Science Basis. Contribution of Working Group I to the Fifth Assessment
711 Report of the Intergovernmental Panel on Climate Change [Stocker, T.F., D. Qin,
712 G.-K. Plattner, M. Tignor, S.K. Allen, J. Boschung, A. Nauels, Y. Xia, V. Bex and P.M.
713 Midgley (eds.)]. Chapter 7. Cambridge University Press, Cambridge, United
714 Kingdom and New York, NY, U, 2013.

715 Colbo, K. and Weller, R. A.: Accuracy of the IMET sensor package in the subtropics. J.
716 Atmos. Oceanic Technol., 26, 1867–1890,
717 <https://doi.org/10.1175/2009JTECHO667.1>, 2009.

718 Collins, W. D., Rasch, P. J., Eaton, B. E., B. Khattatov, V., Lamarque, J-F. and Zender, C.
719 S.: Simulating aerosols using a chemical transport model with assimilation of
720 satellite aerosol retrievals: Methodology for INDOEX. J. Geophys. Res., 106 (D7),
721 7313–7336, 2001.

722 d' Almeida, G. A., P. Koepke and E. P. Shettle: Atmospheric Aerosols: Global
723 Climatology and Radiative Characteristics. A. Deepak Publishing, 561 pp. 1991

724 Driemel, A., and Co-authors: Baseline Surface Radiation Network (BSRN): structure and
725 data description (1992–2017), Earth Syst. Sci. Data, 10, 1491-1501,
726 [doi:10.5194/essd-10-1491-2018](https://doi.org/10.5194/essd-10-1491-2018). 2018

727 Emmons, L. K., and co-authors: Description and evaluation of the Model for Ozone and
728 Related chemical Tracers, version 4 (MOZART-4), Geosci. Model Dev., **3**, 43–67.
729 www.geosci-model-dev.net/3/43/2010/, 2010.

730 Fu, Q. and Liou, K-N.: Parameterization of the radiative properties of cirrus clouds, J.
731 Atmos. Sci., 50, 2008–2025, 1993.

732 Fu, Q., Lesins, G., Higgins, J., Charlock, T., Chylek, P. and Michalsky, J.: Broadband
733 water vapor absorption of solar radiation tested using ARM data. *Geophys. Res. Let.*,
734 25, 1169–1172, 1998.

735 Ginoux, P., Chin, M., Tegen, I., Prospero, J. M., Holben, B., Dubovik, O. and Lin, S-J.:
736 Sources and distributions of dust aerosols simulated with the GOCART model *J. of*
737 *Geophys. Res.: Atmos.*, 106, 20255-20273, doi.org/10.1029/2000JD000053, 2001.

738 Haeffelin, M., Kato, S., Smith, A. M., Rutledge, C. K., Charlock T. P. and Mahan, J. R.:
739 Determination of the thermal offset of the Eppley precision spectral pyranometer,
740 *Appl. Opt.* 40, 472-484, 2001.

741 Ham, S., Kato, S. and Rose, F. G.: Examining biases in diurnally-integrated shortwave
742 irradiances due to two- and four-stream approximations in cloudy atmosphere. *J.*
743 *Atmos. Sci.*, 77(2), 551–581. doi: 10.1175/JAS-D-19-0215.1, 2020.

744 Hess, M., Koepke, P. and Schult, I.: Optical Properties of Aerosols and Clouds: The
745 software package OPAC. *Bull. Amer. Meteor. Soc.*, 79, 831-844.
746 [https://doi.org/10.1175/1520-0477\(1998\)079<0831:OPOAAC>2.0.CO;2](https://doi.org/10.1175/1520-0477(1998)079<0831:OPOAAC>2.0.CO;2), 1998.

747 Holben B.N., Eck, T. F., Slutsker, I., Tanre, D., Buis, J. P., Setzer, A., Vermote, E.,
748 Reagan, J. A., Kaufman, Y., Nakajima, T., Lavenu, F., Jankowiak, I. and Smirnov,
749 A.: AERONET - A federated instrument network and data archive for aerosol
750 characterization, *Rem. Sens. Environ.*, 66, 1-16, 1998

751 Hsu, N. C., Tsay, S-C, King, M. D. and Herman, J. R.: Deep Blue Retrievals of Asian
752 Aerosol Properties During ACE-Asia, *IEEE Trans. On Geosci. and Rem. Sens.*,
753 44(11), 2006.

754 Huneus, N., and co-authors: Global dust model intercomparison in AeroCom phase I,
755 Atmos. Chem. Phys., 11, 7781–7816. www.atmos-chem-phys.net/11/7781/2011/
756 [doi:10.5194/acp-11-7781-2011](https://doi.org/10.5194/acp-11-7781-2011), 2011.

757 Kato, S., Loeb, N. G., Rose, F. G., Doelling, D. R., Rutan, D. A., Caldwell, T. E., Yu L.
758 and Weller, R. A.: Surface irradiances consistent with CERES-derived top-of-
759 atmosphere shortwave and longwave irradiances. J. of Clim Dyn. doi: 10.1175/JCLI-
760 D-12-00436, 2013.

761 Kato, S., Rose, F. G., Rutan, D. A., Thorsen, T. J., Loeb, N. G., Doelling, D. R., Huang,
762 X., Smith, W. L., Su, W. and Ham, S-H.: Surface Irradiances of Edition 4.0 Clouds
763 and the Earth’s Radiant Energy System (CERES) Energy Balanced and Filled
764 (EBAF) Data Product. J. of Clim Dyn. doi: 10.1175/JCLI-D-17-0523.1, 2018.

765 Kaufman, Y. and co-authors: A critical examination of the residual cloud contamination
766 and diurnal sampling effects on MODIS estimates of aerosol over ocean, IEEE Trans.
767 Geosci. Rem. Sens. 43, DOI: 10.1109/TGRS.2005.858430, 2005.

768 Kinne, S. and co-authors: An AeroCom initial assessment – optical properties in aerosol
769 component modules of global models. Atmos. Chem. Phys., 6, 1815–1834.
770 www.atmos-chem-phys.net/6/1815/2006/, 2006.

771 Koch, D., and co-authors: Evaluation of black carbon estimations in global aerosol
772 models. Atmos. Chem. Phys., 9, 9001–9026. [www.atmos-chem-](http://www.atmos-chem-phys.net/9/9001/2009/)
773 [phys.net/9/9001/2009/](http://www.atmos-chem-phys.net/9/9001/2009/), 2009.

774 L’Ecuyer T. S., Beadoing, H. K., Rodell, M., Olson, W., Lin, B., Kato, S., Clayson, C.
775 A., Wood, E., Sheffield, J., Adler, R., Huffman, G., Bosilovich, M., Gu, G.,
776 Robertson, F., Houser, P. R., Chambers, D., Famiglietti, J. S., Fetzer, E., Liu, W. T.,

777 Gao, X., Schlosser, C. A., Clark, E., Lettenmaier, D. P. and Hilburn, K.: The
778 observed state of the energy budget in the early twenty-first century. *J Clim*
779 28(21):8319–8346. <https://doi.org/10.1175/Jcli-D-14-00556.1>, 2015.

780 Levy, R. C., Remer, L. A., Kleidman, R. G. , Mattoo, S., Ichoku, C., Kahn R. and Eck, T.
781 F.: Global evaluation of the collection 5 MODIS dark-target aerosol products over
782 land. *Atmos. Chem and Phys.*, 10, 103999-10420. [https://doi.org/10.5194/acp-10-](https://doi.org/10.5194/acp-10-10399-2010)
783 10399-2010, 2010.

784 Levy, R. C., Mattoo, S., Munchak, L. A., Remer, L. A., Sayer, A. M., Patadia, F. and
785 Hsu, N. C.: The Collection 6 MODIS aerosol products over land and ocean. *Atmos.*
786 *Meas. Tech.*, 6, 2989-3034, [10.5194/amt-6-2989-2013](https://doi.org/10.5194/amt-6-2989-2013), 2013.

787 Liousse, C., Penner, J. E., Chuang, C., Walton, J. J., Eddleman, H. and Cachier, H.: A
788 global three-dimensional model study of carbonaceous aerosols, *J. Geophys. Res. A.*,
789 101(D14), 19 411– 19 432, 1996.

790 Loeb, N. G., Kato, S., Loukachine, K. and Smith, N. M.: Angular Distribution Models for
791 Top-of-Atmosphere Radiative Flux Estimation from the Clouds and the Earth's
792 Radiant Energy System Instrument on the Terra Satellite. Part I: Methodology, *J.*
793 *Atmos. Oceanic Technol*, 22, 338-351, 2005.

794 Loeb, N. G. and Su, W.: Direct Aerosol Radiative Forcing Uncertainty Based on a
795 Radiative Perturbation Analysis. *J. Climate*, 23(19), 5288-5293. doi:
796 10.1175/2010JCLI3543.1, 2010.

797 Loeb, N. G., Doelling, D. R., Wang, H., Su, W., Nguyen, C., Corbett, J. G., Liang, L., Mitrescu,
798 C., Rose, F. G. and Kato, S.: Clouds and the Earth's Radiant Energy System (CERES)
799 Energy Balanced and Filled (EBAF) top-of-atmosphere (TOA) Edition-4.0 data

800 product. *J. Climate*, 31, 895–918, <https://doi.org/10.1175/JCLI-D-17-0208.1>,
801 2018.

802 Loeb, N. G., Rose, F. G., Kato, S., Rutan, D. A., Su, W., Wang, H., Doelling, D. R., Smith, W.
803 L. and Gettelman, A.: Toward a Consistent Definition between Satellite and Model
804 Clear-Sky Radiative Fluxes, *J. Clim.* DOI: 10.1175/JCLI-D-19-0381.1, 2020.

805 Long, C. N., Ackerman, T. P., Gaustad, K. L. and Cole, J. N. S.: Estimation of fractional
806 sky cover from broadband shortwave radiometer measurements, *J. Geophys.*
807 *Res.*,111, D11204, doi:10.1029/2005JD006475, 2006.

808 Martins, J. V., D. Tanre, D., Remer, L., Kaufman, Y., Mattoo, S. and Levy, R.: MODIS cloud
809 screening for remote sensing of aerosols over oceans using spatial variability,
810 *Geophys. Res. Lett.*, 29, 1619, DOI:10.1029/2001GL013252, 2002.

811 Marshak, A., Ackerman, A., da Silva, A. M., Eck, T., Holben, B., Kahn, R., Kleidman, R.,
812 Knobelspiesse, K., Levy, R., Lyapustin, A., Oreopoulos, L, Remer, L., Torres, O.,
813 Várnai, T., Wen, G., and Yorks, J.: Aerosol properties in cloudy environments from
814 remote sensing observations, *Bul. Amer. Met. Soc.*, 102, E2177–E2197,
815 <https://doi.org/10.1175/BAMS-D-20-0225.1>, 2021.

816 McPhaden, M. J.: TAO/TRITON tracks Pacific Ocean warming in early 2002. *CLIVAR*
817 *Exchanges*, No. 24, International CLIVAR Project Office, Southampton, United
818 Kingdom, 7–9, 2002.

819 #—, and Coauthors: RAMA: The Research Moored Array for African–Asian–
820 Australian Monsoon Analysis and Pre- diction. *Bull. Amer. Meteor. Soc.*, 90, 459–
821 480, doi:10.1175/ 2008BAMS2608.1, 2009.

822 Michalsky, J. J., Gueymard, C., Kiedron, P., McArthur, L. J. B., Philipona, R. and
823 Stoffel, T.: A proposed working standard for the measurement of diffuse horizontal
824 shortwave irradiance. *J. of Geophys. Res. A.*, 112(D16),
825 <https://doi.org/10.1029/2007JD008651>, 2007.

826
827 Minnis, P., Sun-Mack, S., Chen, Y., Chang, F., Yost, C. R., Smith, W. L., Heck, P. W.,
828 Arduini, R. F., Bedka, S. T., Yi, Y., Hong, G., Jin, Z., Painemal, D., Palikonda, R.,
829 Scarino, B. R., Spangenberg, D. A., Smith, R. A., Trepte, Q. Z., Yang, P. and Xie, Y.:
830 CERES MODIS Cloud Product Retrievals for Edition 4–Part I: Algorithm Changes.
831 *IEEE Transactions on Geoscience and Remote Sensing*, 1-37. doi:
832 [10.1109/TGRS.2020.3008866](https://doi.org/10.1109/TGRS.2020.3008866), 2020.

833 Ohmura A., Dutton, E., Forgan, B., Frohlich, C., Gilgen, H., Hegne, H., Heimo, A., Konig-
834 Langlo, G., McArthur, B., Muller, G., Philipona, R., Whitlock, C., Dehne, K. and Wild,
835 M.: Baseline Surface Radiation Network (BSRN/WCRP): New precision
836 radiometry for climate change research. *Bull. Amer. Meteor. Soc.*, 79, No. 10,
837 2115-2136, 1998.

838 Randles, C. A., Da Silva, A. M., Buchard, V., Colarco, P. R., Darmenov, A., Govindaraju,
839 R., Smirnov, A., Holben, A., Ferrare, R., Hair, J., Shinozuka, Y. and Flynn, C. J.: The
840 MERRA-2 aerosol reanalysis, 1980 onward. Part I: System description and data
841 assimilation evaluation, *J. Clim.* 30(17), [http://dx.doi.org/10.1175/JCLI-D-16-](http://dx.doi.org/10.1175/JCLI-D-16-0609.s1)
842 [0609.s1](http://dx.doi.org/10.1175/JCLI-D-16-0609.s1), 2017.

843 Rasch, P. J., Mahowald, N. M. and Eaton, B. E.: Representations of transport,
844 convection, and the hydrologic cycle in chemical transport models: Implications
845 for the modeling of short-lived and soluble species. *J. of Geo. Res.*, 102, 127-138,

846 1997.

847 Rasch, P. J., Collins, W. D. and Eaton, B. E.: Understanding the Indian Ocean
848 Experiment (INDOEX) aerosol distributions with an aerosol assimilation. *J. of*
849 *Geo. Res.*, 106, 7337-7355, 2001.

850 Remer, L. A., and Co-authors: The MODIS aerosol algorithm, products, and validation. *J.*
851 *Atmos. Sci.*, 62, 947–973, 2005.

852 Remer, L. A., Kleidman, R. G., Levy, R. C., Kaufman, Y. J., Tanre, D., Mattoo, S.,
853 Vanderlei Martins, J., Ichoku, C., Koren, I., Yu, H. and Holben, B. N.: Global aerosol
854 climatology from the MODIS satellite sensors. *J. Geophys. Res.: A*. 113(D14),
855 <https://doi.org/10.1029/2007JD009661>, 2008.

856 Rose, F. G, Rutan, D. A., Charlock, T., Smith, G. L. and Kato, S.: An Algorithm for the
857 Constraining of Radiative Transfer Calculations to CERES-Observed Broadband
858 Top-of-Atmosphere Irradiance. *J. Atmos. and Ocean. Tech.* 30, 1091-1106. DOI:
859 10.1175/JTECH-D-12-00058.1, 2013.

860 Rutan, D., Rose, F., Roman, M., Manalo-Smith, N., Schaaf, C. and Charlock, T.:
861 Development and assessment of broadband surface albedo from Clouds and the
862 Earth's Radiant Energy System clouds and radiation swath data product. *J. Geophys.*
863 *Res.*, 114, D08125. doi:10.1029/2008JD010669, 2009.

864 Rutan, D., Kato, S., Doelling, D. R., Rose, F. G., Nguyen, L. T. and Caldwell, T.: CERES
865 Synoptic Product: Methodology and Validation of Surface Radiant Flux. *J. Atmos.*
866 *And Ocean. Tech.*, 32, doi:10.1175/JTECH-D-14-00165.1, 2015.

867 Servain, J., Busalacchi, A. J., McPhaden, M. J., Moura, A. D., Reverdin, G., Vianna, M.
868 and Zebiak, S. E.: A Pilot Research Moored Array in the Tropical Atlantic

869 (PIRATA). Bull. Amer. Meteor. Soc., 79, 2019–2031, doi:10.1175/1520-
870 0477(1998)079,2019:APRMAI.2.0.CO;2. 1998

871 Sinyuk, A., Torres, O. and Dubovik, O.: Combined use of satellite and surface
872 observations to infer the imaginary part of refractive index of Saharan dust.
873 Geophysical Research Letters, 30(2), 1081. <https://doi.org/10.1029/2002GL016189>,
874 2003.

875 Smirnov, A., Holben, B. N., Eck, T. F., Dubovik, O. and Slutsker, I.: Cloud-screening
876 and quality control algorithms for the AERONET database. Rem. Sens. Env. 73, 337-
877 349, 2000.

878 Soden, B. and Chung, E-S.: The Large-Scale Dynamical Response of Clouds to Aerosol
879 Forcing. J. of Climate, 30, 8783-8794. doi: [https://doi.org/10.1175/JCLI-D-17-](https://doi.org/10.1175/JCLI-D-17-0050.1)
880 [0050.1](https://doi.org/10.1175/JCLI-D-17-0050.1), 2017.

881 Stephens, G. L., Slingo, J. M., Rignot, E., Reager, J. T., Hakuba, M. Z., Durack, P. J.,
882 Worden, J. and Rocca, R.: Earth's water reservoirs in a changing climate. Proc. R.
883 Soc. A 476: 20190458. <http://dx.doi.org/10.1098/rspa.2019.0458>, 2020.

884 Su, W., Schuster, G. L., Loeb, N. G., Rogers, R. R., Ferrare, R. A., Hostetler, C. A., Hair,
885 J. W., and Obland, M. D.: Aerosol and cloud interaction observed from high spectral
886 resolution lidar data. J. of Geophys. Res.: Atmos., 113(D24), D24202.
887 Doi:10.1029/2008JD010588, 2008.

888 Su, W., Corbett, J., Eitzen, Z. and Liang, L.: Next-generation angular distribution models
889 for top-of-atmosphere radiative flux calculation from CERES instruments:
890 methodology. Atmos. Meas. Tech., 8(2), 611-632. doi: 10.5194/amt-8-611-2015,
891 2015.

892 Su, W., Corbett, J., Eitzen, Z. and Liang, L.: Next-generation angular distribution models
893 for top-of-atmosphere radiative flux calculation from CERES instruments: validation.
894 Atmos. Meas. Tech., 8(8), 3297-3313. doi: 10.5194/amt-8-3297-2015, 2015.

895 Su, W., G. L. Schuster, N. G. Loeb, R. R. Rogers, R. A. Ferrare, C. A. Hostetler, J. W.
896 Hair, M. D. Obland, 2008: Aerosol and cloud interaction observed from high spectral
897 resolution lidar data. J. of Geophys. Res., Atmos., 113(D24), D24202.
898 Doi:10.1029/2008JD010588.

899 Textor, C. and Co-authors: Analysis and quantification of the diversities of aerosol
900 life cycles within AeroCom, Atmos. Chem. Phys., 6, 1777-1813. [www.atmos-](http://www.atmos-chem-phys.net/6/1777/2006/)
901 [chem-phys.net/6/1777/2006/](http://www.atmos-chem-phys.net/6/1777/2006/), 2006.

902 Textor, C., and Co-authors: The effect of harmonized emissions on aerosol
903 properties in global models – an AeroCom experiment. Atmos. Chem. Phys., 7,
904 4489–4501. www.atmos-chem-phys.net/7/4489/2007/, 2007.

905 Varnai, T., Marshak, A. and Eck, T. F.: Observation-based study on aerosol optical depth
906 and particle size in partly cloudy regions. J. Geophys. Res: A. 122, 10,013–10,024,
907 <https://doi.org/10.1002/2017JD027028>, 2017.

908 Wen, G., Marshak, A., Cahalan, R. F., Remer, L. A. and Kleidman, R. G.: 3-D aerosol-
909 cloud radiative interaction observed in collocated MODIS and ASTER images of
910 cumulus cloud fields, J. Geophys. Res., 112, D13204, doi:10.1029/2006JD008267,
911 2007.

912 Wielicki, B. A., Barkstrom, B. R., Harrison, E. F., Lee, R. B. III, Smith, G. L. and Cooper, J.
913 E.: Clouds and the Earth's Radiant Energy System (CERES): An Earth Observing
914 System Experiment. Bull. Amer. Meteor. Soc., 77, 853-868, 1996.

915 Zender, C. S., Huishen, B. and Newman, D.: Mineral Dust Entrainment and Deposition
916 (DEAD) model: Description and 1990s dust climatology. *J. Geophys. Res.*, 108,
917 doi:10.1029/2002JD002775, 2003.